Universiteit Antwerpen

This item is the archived peer-reviewed author-version of:

Recent trends in plasmon-assisted photocatalytic CO₂ reduction

Recent Trends in Plasmon-Assisted Photocatalytic CO_2 Reduction

Radu-George Ciocarlan,[a] Natan Blommaerts,[a][b][c] Silvia Lenaerts,[b][c] and Pegie Cool,*[a] Sammy W. Verbruggen*[b][c]

[a]   Dr. R-G. Ciocarlan, Dr. N. Blommaerts, Prof. P. Cool
        Department of Chemistry
        University of Antwerp
        Universiteitsplein 1, 2610 Wilrijk, Belgium
        E-mail: Pegie.Cool@uantwerpen.be
                Sammy.Verbruggen@uantwerpen.be
[b]   Dr. N. Blommaerts, Prof. S. Lenaerts, Prof. S. W. Verbruggen
        Department of Bioscience Engineering
        University of Antwerp
        Groenenborgerlaan 171, 2020 Antwerp, Belgium
[c]   Dr. N. Blommaerts, Prof. S. Lenaerts, Prof. S. W. Verbruggen
        NANOlab Center of Excellence
        University of Antwerp
        Groenenborgerlaan 171, 2020 Antwerp, Belgium
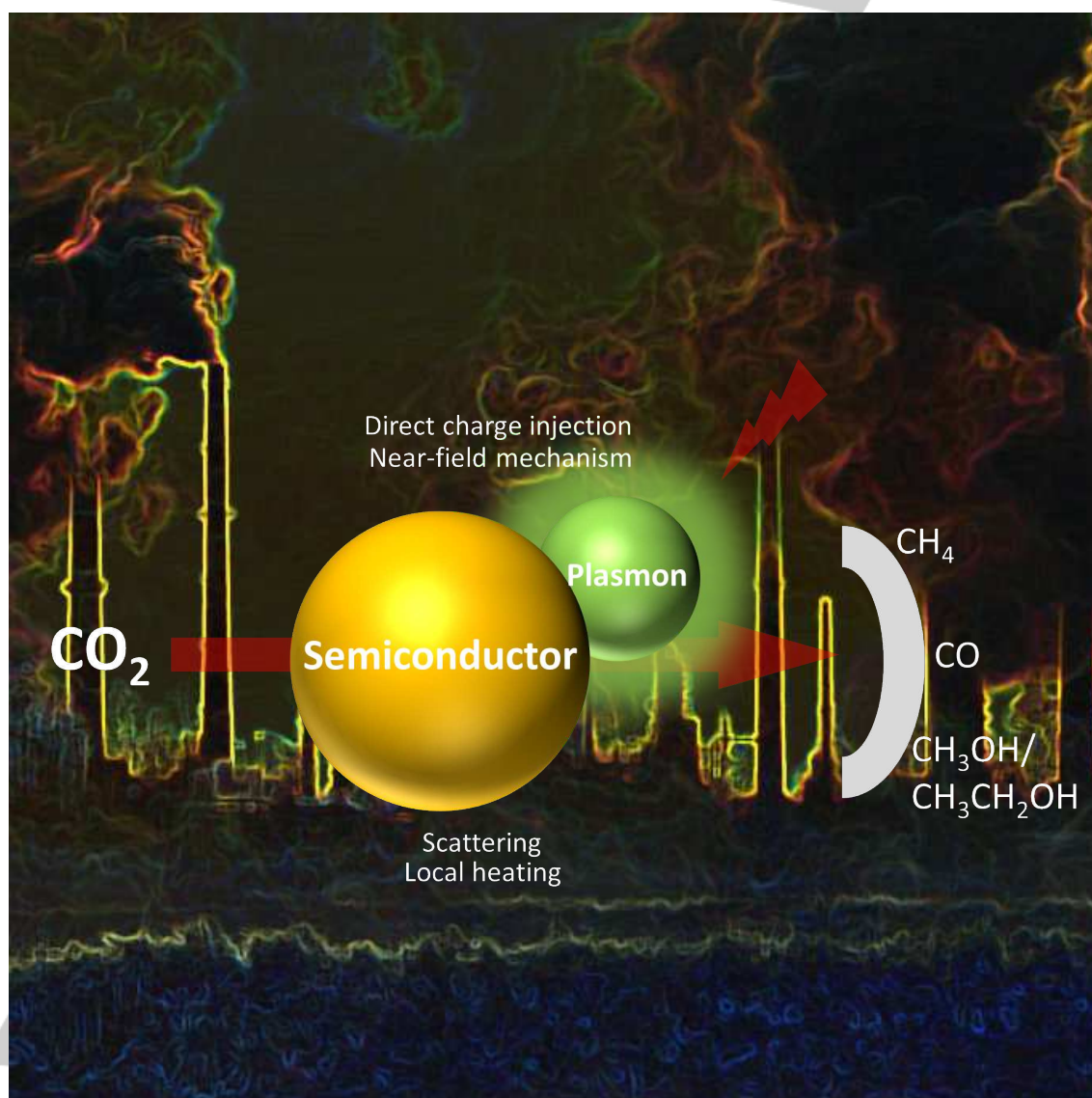
Abstract: Direct photocatalytic reduction of CO_2 has become a wide field of research. It is thus of utmost importance to maintain an overview of the various materials used to sustain this process, find common trends, and in this way eventually improve the current conversion and selectivity yields. In particular, CO_2 photoreduction using plasmonic photocatalysts under solar light has gained tremendous attention, and a wide variety of materials has been developed to reduce CO_2 towards more practical gases or liquid fuels (CH_4, CO, CH_3OH/CH_3CH_2OH) in this manner. This review therefore aims at providing insights in current developments of photocatalysts consisting of only plasmonic nanoparticles and semiconductor materials. By classifying recent studies based on product selectivity, this review aims to unravel common trends that can provide effective information on ways to improve the photoreduction yield or possible means to shift the selectivity towards desired products, thus generating new ideas for the way forward.

Pegie Cool received her PhD degree in Science, Chemistry in 1998 at the University of Antwerp, Belgium. During her postdoctoral fellowship funded by the Research Foundation Flanders, she was associated at the Texas A&M University, USA and at the University of Queensland, Australia. In 2004 she was appointed Assistant Professor and since 2012 she is Full Professor and head of the Laboratory of Adsorption and Catalysis at the Chemistry Department in Antwerp. Her main expertise is on the development of inorganic nanoporous materials, involving pore size modification and activation for sorption and (photo)catalysis. The main focus is on environmental applications, such as wastewater purification, CO_2 conversion, and automotive exhaust gas conversion. She is Board of Directors member of the European Nanoporous Materials Institute of Excellence (ENMIX aisbl) and Board Member of the Dutch Zeolite Association (Netherlands-Flanders).

Sammy W. Verbruggen received his M.Sc. in Bioscience Engineering: Catalysis from KU Leuven, Belgium in 2010. In 2014 he received a joint PhD degree from the University of Antwerp and KU Leuven for his multidisciplinary work on gas phase photocatalysis, for which he was granted the Belgian Industrial R&D Award. After a postdoctoral fellowship funded by the Research Foundation Flanders (FWO), he was appointed as Assistant Professor at the University of Antwerp in 2019. His research group focuses on fundamentals and applications of plasmonic photocatalysis for energy and environment. Research lines include the synthesis of new plasmonic nanostructures, and their application in CO_2 conversion, air purification, H_2 production and self-cleaning surfaces.

1. The global (CO_2) problem

These days, there cannot be any denying concerning climate change and greenhouse effects. The ever-increasing CO_2 concentration in our atmosphere as a direct consequence of human activities is the main cause for global warming. Although there are stronger greenhouse gasses than CO_2, such as methane, it is estimated that CO_2 contributes for 63% to the global warming effect. The fact that the CO_2 concentration has increased by 40% upon further industrialization is definitely no coincidence. Figure **1** shows the CO_2 concentration (in ppm) since 1960 according to the National Oceanic and Atmospheric Administration (NOAA). It is clear from this figure that there is a steep rise in concentration from below 320 ppm to nearly 420 ppm. The main source of CO_2 emissions is the combustion of fossil fuels such as coal, oil or natural gas, providing the majority of worldwide energy.[1-6] It is even predicted by BP's energy outlook that the predominant energy source until 2030 will still be oil.[7] According to the Intergovernmental Panel on Climate Change (IPCC), CO_2 concentrations in our atmosphere can reach 590 ppm by 2100, leading to global temperature increase of 1.9°C. Melting of polar ice is not the only consequence of this temperature increase, changing weather conditions including storms, floods, or wildfires can have severe effects on both fauna and flora.[8,9]

Not only the CO_2 concentration has been steeply increasing since the industrial revolution but also the world population has been increasing rapidly since the 1900's, reaching seven billion people on October 31th 2011 and almost 7.8 billion in the beginning of 2020. As a consequence, also the global power consumption increased significantly from 15 TW in 2010 and predicted to reach 27 TW in 2050.[1,4–6] Therefore, many efforts have been made to develop renewable energy sources to meet the demands and to cut the use of fossil fuels. It is estimated, however, that the combined share of renewable energy coming from wind, geothermal, tidal and biomass sources can generate a power of at most 20 TW.[10] A source of energy that is regarded as infinite, however, is solar radiation. In one year, the sun provides the earth with a power of 120 000 TW.[1,5,6,11–13] This means that the amount
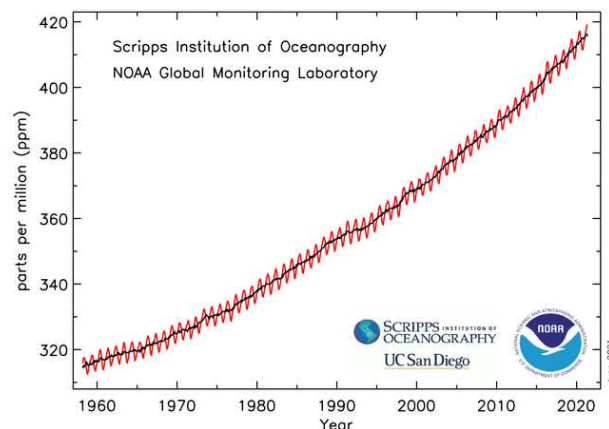
Figure 1. Atmospheric CO_2 concentration at Mauna Loa observatory. The red curve represents the values per month; the black curve takes into account the average seasonal cycle.

that reaches earth in one hour, even exceeds the annual global energy demand. There clearly lies a major potential in using the energy of the sun as sustainable energy source.

Various technologies are being developed for carbon capture and storage such as scrubbing, mineral carbonation, geological or ocean injection. These technologies, however, are expensive and have a great risk of CO_2 leakage.[7] One of the major issues in the development of a suitable CO_2 reduction technology is the stability of the CO_2 molecule. This is mainly due to the C=O double bond, having a binding energy of $750 - 800$ kJ/mol, which is much stronger compared to the C–C (336 kJ/mol) or C–O (327 kJ/mol) single bonds.[14,15] Due to this high energy demand, it would be most useful to harvest the required energy from an infinite and sustainable source: sunlight. The process in which (solar) light is used to activate a catalyst is called photocatalysis. The last decade, photocatalytic CO_2 reduction has gained a lot of interest as can be seen from the sharp increase around 2010 in the amount of publications on this topic.

After a general description of photocatalysis, the review aims to connect and compare a series of CO_2 photoreduction studies. Herein, the focus as well as the novelty of the comprehensive overview lies on three aspects: (i) the selection of scientific papers that are solely and explicitly discussing plasmonic NPs-semiconductors systems involved in CO_2 reduction processes, (ii) the classification of these studies based on the formed reaction products, which intends to ease the work of the reader targeting specific end products, and (iii) the interlink between the different studies, for a better understanding of the photo-assisted mechanisms.

2. Introduction on photocatalysis

Photocatalysis is the process in which light acts as the stimulus for a catalyst to drive a chemical reaction. This domain includes a large range of reactions such as dehydrogenations, oxidations, metal deposition, gaseous pollutant removal, water detoxification and many more. These reactions can be carried out in the gas phase, aqueous phase as well as in organic media.[16] In general, a photocatalytic reaction can be summarized as shown in (eq. 1).[17]

$$(Ox_1)_{ads} + (Red_2)_{ads} \xrightarrow[E_{photon} \geq E_g]{Photocatalyst} Red_1 + Ox_2 \qquad \text{(eq. 1)}$$
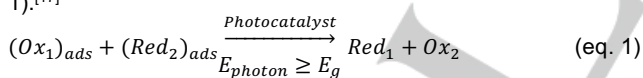
(Ox$_1$)$_{ads}$ – Oxidant 1 adsorbed; (Red$_2$)$_{ads}$ – Reductor 2 adsorbed; Red$_1$ – Reductor 1; Ox$_2$ – Oxidant 2; E$_{photon}$ – Photon energy (eV); E$_g$ – Band-gap energy.

With E_g the band gap energy of the semiconductor and E_{photon} the energy of the incident light.

The overall heterogeneous photocatalytic process can be described in five independent steps: (1) diffusion of reactants to the surface, (2) adsorption, (3) reaction in the adsorbed phase, (4) desorption, (5) diffusion of the products. The actual photocatalytic reaction occurs in the adsorbed phase and is similar to conventional heterogeneous catalysis except for the activation mode of the catalyst, which is usually thermal in nature for conventional catalysis and photonic for photocatalysis. The catalyst is activated through the absorption of a photon with an energy larger than the band gap. This photon absorption results in the excitation of a negatively charged electron (e-) from the valence band to the conduction band, leaving a positively charged hole (h+) in the valence band. This charge separation has to be sufficiently stable, *i.e.* it has to compete with recombination processes that can occur in the bulk as well as at the surface of the catalyst particle. These recombination processes will lead to a lowered overall efficiency. After the generation of an e--h+ pair, the charges have to diffuse to the surface of the catalyst particle where they initiate reduction and oxidation reactions.[16–18] The main processes which occur in a semiconductor particle are summarized in Figure **2**.
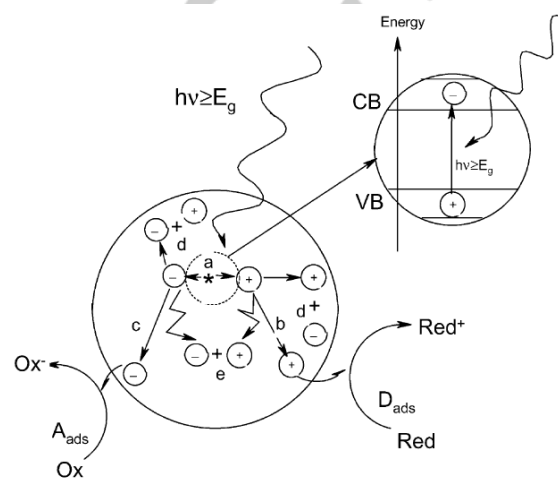
Figure 2. Main processes occurring on a semiconductor particle: (a) e--h+ pair generation; (b) oxidation of an adsorbed electron donor (D$_{ads}$); (c) reduction of an adsorbed electron acceptor (A$_{ads}$); (d) e--h+ pair recombination at the surface and (e) e--h+ pair recombination in the bulk. Reprinted with permission from ref.[17]

A photocatalyst is typically a semiconductor material which is ideally photostable, non-toxic, easy to process and cheap. Titanium dioxide (TiO_2) is the most common semiconductor photocatalyst which satisfies the above-mentioned requirements. TiO_2 is an n-type semiconductor due to oxygen vacancies according to (eq. 2).

$$O_O^x \xrightarrow{TiO_2} V_O^{\bullet\bullet} + 2e^- + \frac{1}{2}O_2(g) \qquad \text{(eq. 2)}$$

This reaction (following the Kröger-Vink notation) states that inside TiO_2, a 2+ positively charged oxide ion vacancy is present due to release of two electrons and molecular oxygen. Heating in an oxygen-free environment can induce this reaction.

Due to different lattice structures between anatase and rutile, causing different densities and electronic band structure, there is a small difference in band gap. The band gap of anatase is 3.20 eV and for rutile 3.02 eV, which both correspond to the UV region of the electromagnetic spectrum.[19] This leads to one of the first major disadvantages of TiO_2, since the entire solar spectrum consists only of *ca*. 5% UV light. This explains the variety of research focusing on shifting the absorption wavelength of TiO_2 from the UV to the visible part of the electromagnetic spectrum.[20] The second disadvantage of TiO_2 is the high recombination rate of generated electrons and holes, before the excited charge carriers can reach the catalyst surface to perform redox reactions. Over the years, different types of metal oxides have shown a similar behaviour to TiO_2, regarding the high recombination rate or lack of activity in the visible region, such as ZnO, CuO, Cu_2O,

NiO, $SrTiO_3$, Fe_2O_3, Bi_2O_3, CdS, SnO_2, WO_3, Bi_2WO_6 etc.[21] Various strategies have been developed to overcome these two major shortcomings, such as doping of metals and non-metals to shift the activity window to the visible part of the spectrum, introducing defects in the lattice to act as charge trapping centres in order to enhance charge separation, or modification with (noble) metal nanoparticles that display (localized) surface plasmon resonance ((L)SPR). In the latter case, the term plasmonic photocatalysis is used, which is the core focus of this review article.

In this review, we will summarize a series of efforts that have been made by the entire community to make progress in the field of plasmonic CO_2 reduction. It is important to note that only plasmon-enhanced photocatalysis will be covered, thus in the presence of a semiconductor as photocatalyst and not direct photo(thermal) catalysis on the nanoparticles itself, in absence of a semiconductor.

3. Plasmonic photocatalysis

SPR occurs when light of a certain wavelength hits a nanoparticle, and induces the free electron cloud to oscillate along with the electric field component of the incident light and against the restoring force of the positive nucleus.[22] Since the electrons move coherently at the same frequency in a very small particle, one side of the surface of the nanoparticle will become partially negatively charged due to the accumulation of electrons at the surface. Conversely, the opposite side will become partially positively charged. In this manner, a dipolar oscillation of the electron cloud is created. This is schematically illustrated in Figure **3**. Higher excitation modes also exist mainly for larger particles, such as the quadrupolar mode in which the electron cloud moves both parallel as well as antiparallel with respect to the applied field.[23]
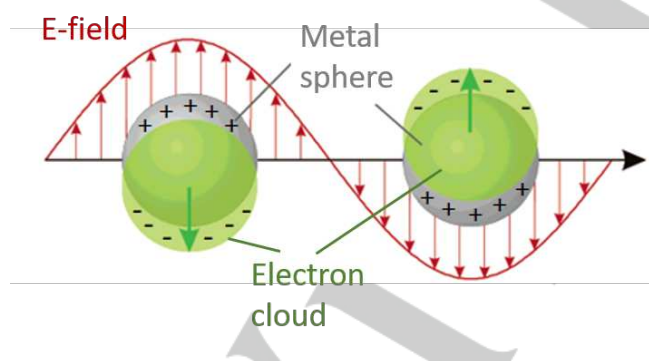
Figure 3. Schematic representation of the surface plasmon resonance phenomenon in a metallic nanoparticle in which the electron cloud oscillates along with the electric field (E-field) component of the incident light and against the restoring force of the positive nucleus. Adapted from ref.[23]

In 1908, Gustav Mie was the first to explain the red color of gold nanoparticle solutions by solving Maxwell's equations for an electromagnetic light wave that interacted with small spheres for which the frequency dependent dielectric constant was the same as for the bulk metal.[24] If the NPs are significantly smaller than the wavelength of light, only the dipole oscillation is important to the extinction cross-section, leading to the following relation shown in (eq. 3).

$$\sigma_{ext}(\omega) = 9\frac{\omega}{c}\varepsilon_m^{3/2}V\frac{\varepsilon_2(\omega)}{[\varepsilon_1(\omega)+2\varepsilon_m]^2+\varepsilon_2(\omega)^2} \qquad \text{(eq. 3)}$$

V is the particle volume, ω is the angular frequency of the exciting light wave, c is the speed of light, ε_m is the dielectric function of the surrounding medium and $\varepsilon(\omega) = \varepsilon_1(\omega) + i\varepsilon_2(\omega)$ the dielectric function of the material itself. When $\varepsilon_1(\omega) = -2\varepsilon_m$ and if ε_2 negligibly dependent on ω, then the resonance condition is regarded to be fulfilled, which is the case for free-electron metals in the UV-Vis range. $\varepsilon_1(\omega)$ is related to the refractive index and the ability of the material to 'slow down' the light, whereas $\varepsilon_2(\omega)$ is related to damping losses, which arise from absorption of the light travelling through the material. The plasmon wavelength is determined by four main factors: the composition of the metal, the size, shape, and the dielectric environment. The peak wavelength of the plasmon resonance is given by the wavelength dependence of $\varepsilon_1(\omega)$ which explains the differences in resonant energy between different metals such as gold and silver. It is important to notice that σ_{ext} varies linearly with the particle volume, while the number density decreases as R^3 increases (with R the radius of the particle). This means that the absorption coefficient does not depend on the particle size. This is only the case for particles smaller than 50 nm. If the particles become larger than 50 nm, scattering effects start to become significant. For very small particles (with a diameter < 5-10 nm), on the other hand, changes in dielectric function and hence in optical properties can be expected since the material properties themselves change. For large NPs (in case of Au larger than *ca.* 20 nm), the dipole approximation is no longer valid. The plasmon resonance in this case will also depend on the particle size. The higher order modes are becoming important as the particle increases further in size since the polarization of the particle is no longer homogeneous. These higher order modes have their absorption maximum at longer wavelengths, which induces a red shift in the plasmon band upon increasing particle size. At the same time, a larger bandwidth is observed if the particle size increases. The bandwidth of the plasmon band is indicative for the dephasing of the coherent electron oscillation. The larger the bandwidth, the faster the electrons lose their coherent motion. From the plasmon bandwidth it has been computed that electron dephasing times are in the order of a few femtoseconds, suggesting that the main relaxation process is due to electron-electron collisions.[25–27]

Incorporation of plasmonic nanoparticles such as Au and Ag in a TiO_2 photocatalyst can be highly beneficial due to the strong SPR properties of these materials that allow a very efficient light absorption over a broad range of the electromagnetic spectrum. In this way, the absorption spectrum of TiO_2 can be extended from the UV region of the spectrum to the visible light range, overcoming one of the major limitations of conventional TiO_2 photocatalysis.[28] Moreover, for particles much smaller than the wavelength of light (< 50 nm), scattering contributions to the total extinction can be neglected. Therefore, absorption is the major contributor. The interesting feature about these particles is that they exhibit absorption cross-sections several times larger than their actual size.[29–31] To exemplify, noble metal nanoparticles of 10 nm can exhibit 10 times higher extinction cross-sections than their geometrical cross-section. At the same time, in the case of Ag NPs this increase is even more extreme and the extinction cross-section can reach 50 times higher values than their geometrical area. It is worth noting that for other metal NPs, like

Cu, the extinction cross-section is considerably lower when compared to the Au or Ag NPs.[30] Hence, if the metals are carefully selected, only small amounts of nanoparticles (in the order of a few wt.%) will already substantially increase the visible light absorption over the entire surface of the photocatalyst. A second benefit is that because of the strong absorption characteristics, almost all incident light will be absorbed at a very small depth from the surface (~10 nm) from the surface, limiting the distance the photogenerated electrons have to travel to reach the surface.[22,32,33] There is also a non-plasmonic effect associated with nanoparticles. If a noble metal and a n-type semiconductor make contact, a Schottky junction is formed, in which an internal electric field is built up (the space charge region) close to the metal-semiconductor interface. Electrons and holes that are created inside the space charge region will be forced to opposite directions due to this built-in field, suppressing electron-hole recombination and thus overcoming the second major limitation of TiO_2 photocatalysis.[22,34,35]

It is important to notice that the actual mechanism behind plasmonic photocatalysis is quite complex, as several, mutually non-exclusive effects may occur. The four most recurring mechanisms that drive plasmonic photocatalysis, *i.e.* direct charge injection, near-field enhancement, scattering, and local heating will be discussed in more detail in the following sections.

3.1. Charge injection from metal to semiconductor

If light of the correct wavelength excites a plasmonic nanoparticle, the energy of the electrons becomes larger than allowed by thermal excitations. As a result, there is no thermodynamic equilibrium with the surrounding atoms, hence the electron is called a 'hot' electron.[36–38] These electrons are excited above the Fermi level of the metal during a non-radiative Landau damping process as illustrated in Figure **4a**. The hot electrons can cover a wide energy range that depends on several factors such as the size and shape of the NPs as well as on the carrier concentration. If the energy of the hot electrons is high enough, *i.e.* higher than the Schottky barrier at the metal-semiconductor interface, they can be injected into the semiconductor (Figure **4b**). This process is energetically favourable in Au/Ag-TiO_2 composites since the height of the Schottky barrier is typically around 1 eV.[39,40] On the other hand, if the energy of the electrons is insufficient, also tunnelling can occur although with a lower possibility.[41,42]

Hot electrons can be regarded as free electrons (with a mean free path in the range of 1-100 nm), that need to reach the metal-semiconductor interface with sufficient energy to overcome the Schottky barrier. However, due to electron-electron and electron-phonon collisions, the hot electrons lose a significant amount of energy. As a consequence, only a small fraction of hot electrons will reach the interface with sufficient energy.[37] A requirement for direct electron injection is that there is direct (electronic) contact between the semiconductor and the plasmonic metal. Typically, in plasmonic photocatalysis research, the bare NPs are simply deposited on top of a photocatalytic film.[29,39,43–51] In this case, only a small fraction of the nanoparticles' surface is in contact with the underlying semiconductor layer. A possible solution is to encapsulate the particles with a TiO_2 shell, or to encapsulate in a semiconductor matrix to make sure that the entire surface of the plasmonic particle is in contact with the photocatalyst.[52]
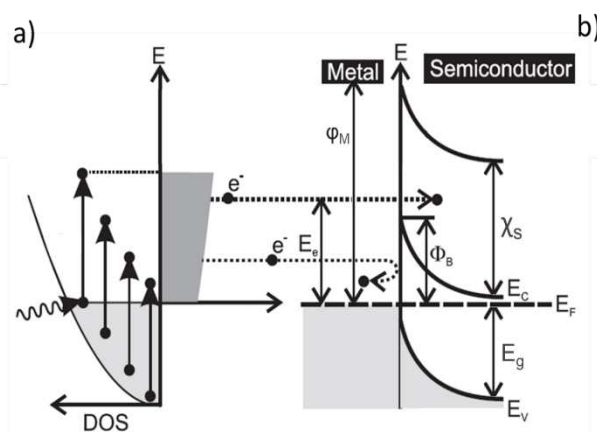
Figure 4. a) Electrons in a metal nanoparticle can be excited above the Fermi level (E_F); b) hot electrons can be injected into the semiconductors conduction band (E_C) if the energy is high enough to overcome the Schottky barrier ($\Phi_B = \varphi_M - \chi_S$), with φ_M the work function of the metal and χ_S the electron affinity of the semiconductor, E_g is the band gap energy, E_v the valence band of the semiconductor, DOS the density of states, and E_{vac} the vacuum energy. Illustration adapted from ref.[38]

3.2. Near-field mechanism

A second important effect that may increase the light efficiency for photocatalysis, is the strong electric near-field enhancement that is generated in the immediate surroundings of a plasmonic nanostructure. Near-field enhancement is a highly local effect, that strongly depends on the size, shape and spatial organization of the nanostructures.[22] Single nanoparticles can already lead to enhancements of the near-electric field up to a factor of 10^3. Multiple nanoparticles in close proximity (with a separation of maximum a few nm) will have enhancements of even a few orders of magnitude higher.

This is because the electric fields start to overlap and form 'hot
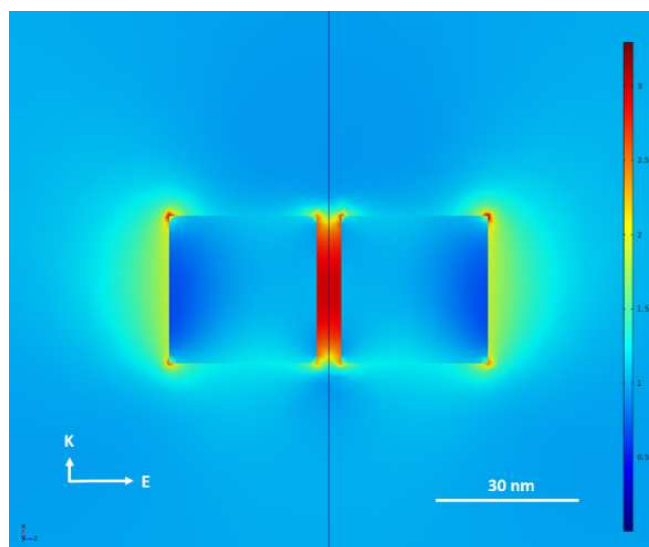
Figure 5. COMSOL simulation of two silver nanocubes separated by a small gap. The near-field enhancement is much stronger between the nanocubes (hot spots) than from a single nanocube.

spots' in which enhancements up to 10^6 can be found according

to literature reports (Figure **5**).[53,54] If a semiconductor is in close proximity to these nanoparticles, the semiconductor will benefit from this concentration of light, leading to significant increases in the rate of electron-hole pair formation.

The efficiency of this so-called 'lens effect' comes with one crucial prerequisite: There has to be an overlap between the SPR energy of the nanoparticle and the band gap energy of the photocatalyst.[22,32]

Not only will there be an increase in the amount of charge carrier formation, the carriers will also be generated much closer to the surface of the photocatalyst which leads to a drastic reduction in charge carrier recombination.[22,55]

between the semiconductors band gap energy and the SPR energy of the nanoparticle is required. This scattering mechanism is mainly important for larger particles (larger than 50 nm).[56]

3.4. Local heating

The last mechanism that will be discussed here is the local heating effect. After electrons and holes are excited in a plasmonic nanostructure, interaction with other electrons in the system can lead to a thermal charge-carrier distribution, *i.e.* not described by a Fermi-Dirac distribution. It takes a few hundred femtoseconds for the thermalization towards a Fermi-Dirac
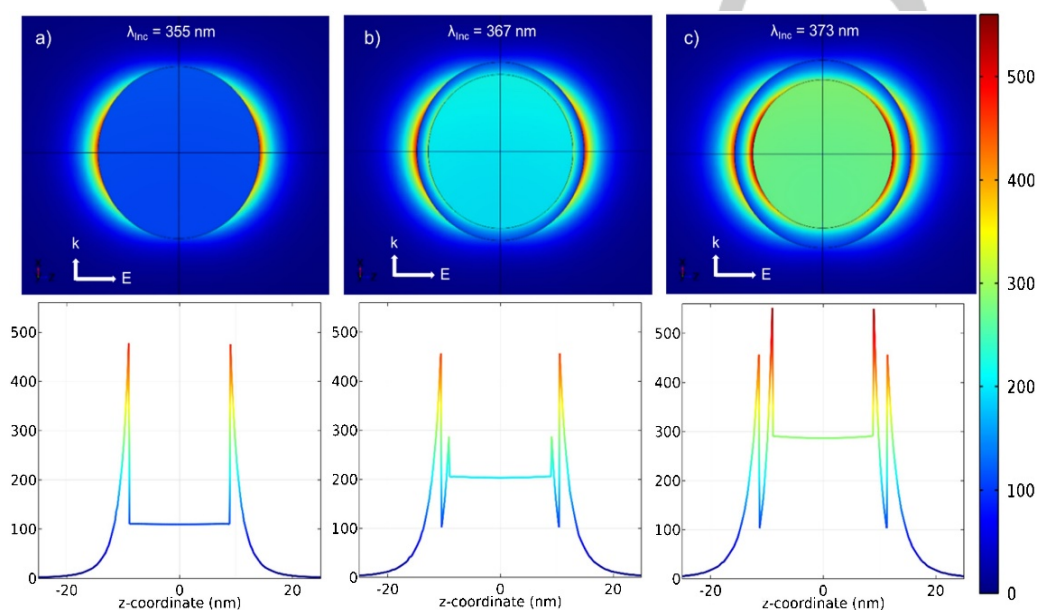
Figure 6. Near-field enhancement ($|E|^2/|E_0|^2$) simulation of a) a bare silver nanoparticle, b) silver nanoparticle encapsulated by a polymer shell of 1.4 nm thickness, c) silver nanoparticle encapsulated by a polymer shell of 2.4 nm thickness. The field enhancement in the direction of polarization is plotted below the corresponding field maps. Reprinted with permission from ref.[49]

The main difference between the direct charge injection and the near-field mechanism is that there is no need for direct contact between the plasmonic particle and the semiconductor in the near-field mechanism, as opposed to the direct charge injection mechanism. This can be seen from Figure **6**, in which the electric field distribution of silver NPs with and without a polymer spacer layer is simulated. It is clear from these images that the near-field also protrudes beyond the nanoparticle surface, even if it is completely covered by a (thin) polymer shell.[49]

It should be noted, however, that the closer to the surface, the stronger the near-field will be. It decays rapidly within a few nanometres away from the surface.

3.3. Scattering

The third important mechanism in plasmonic enhancement is the scattering mechanism. When a plasmonic particle is excited, it can relax via a radiative decay mechanism. These re-emitted or scattered photons can be absorbed again by the semiconductor. This is also called the 'mirror effect', as it seems that the plasmonic particles enhance the optical path length of the photons and give the semiconductor more chance to absorb light and to convert in the excitation of charge carriers. It is important that the energy of the re-emitted photons is sufficient to induce the excitation of charge carriers, implicating that an energy match

distribution. After this thermalization, electrons are cooled down due to energy transfer to phonon modes of the nanoparticle. This occurs within a few picoseconds and leads to an increase in the temperature of the nanoparticle. This heat is dissipated to the environment over longer timescales. As for the classical catalytic systems, even a slight increase of temperature (1 to 10 K) may have an impact on the reaction rate, one can assume a similar behaviour for the photocatalytic systems. However, due to the fast heating dissipation, a greater impact of temperature change is observed for the very small nanoparticles (< 5 nm) or for isolated catalytic sites.[57–65] Shao *et al.* achieved a temperature slightly higher than 300 °C (370-1040 nm light irradiation), which caused the activation of CO_2 and decomposition of H_2 molecules, thus enhancing the photoreduction.[66] At the same time, if the local heating temperature reached is high enough (laser induced, up to 600 °C), the thermal effect can have a great impact and the overall process may be thermally-driven.[67]

4. Plasmon-enhanced photocatalytic CO₂ reduction

Plasmonic photocatalysis is still a relatively 'new' research field. The term was officially introduced by Awazu *et al.* in 2008, although earlier reports, already hinted at this strategy to enhance
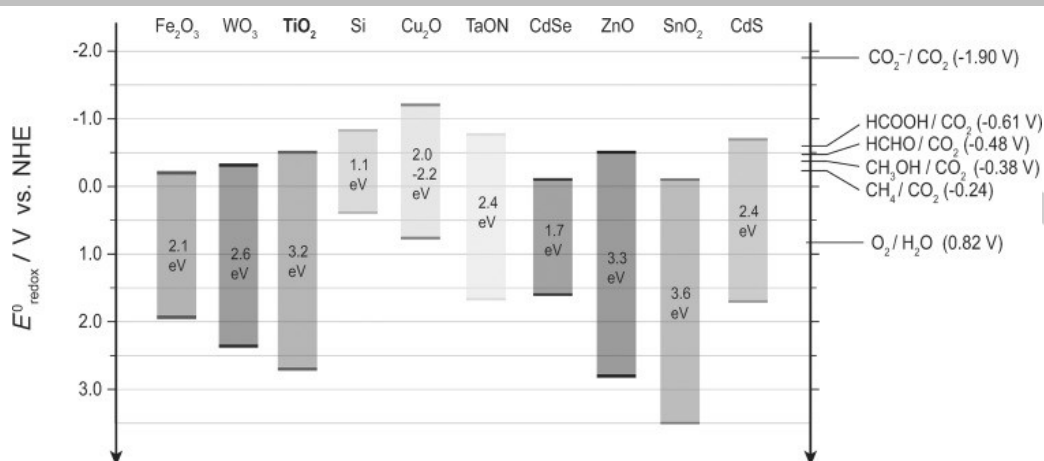
Figure 7. Band positions of different semiconducting materials relative to the redox potentials at pH 7. Reprinted with permission from ref.[1]

photocatalytic activity but no real explanation or mechanism could be provided.[68–70] A lot of effort has been put into extending the absorbance spectrum of a typical photocatalyst such as TiO_2 from the UV to the UV-Vis part of the electromagnetic spectrum using plasmonics.[33,43,49,51,52,71–78] This is especially important if it is aimed at using sunlight.

4.1. General mechanism of photocatalytic CO_2 reduction

The mechanism behind photocatalytic CO_2 conversion is a very complex process that involves multiple bond breaking and formation steps, usage of up to eight electrons and holes, and depending on the used materials and experimental conditions, a range of different intermediate products can be formed. Therefore, understanding of the underlying mechanism is of crucial importance for achieving improvements in CO_2 reduction, mainly on two levels. First of all, a better understanding of the mechanism can increase the overall activity and thus the conversion rate of CO_2 by minimizing thermodynamic and kinetic barriers of the relevant reactions. Secondly, selectivity should be controlled since the number of possible reaction products is large, so that the reaction can be tuned towards the desired end product such as CH_4 or CO. There is still a lot of debate going on over the exact mechanism of photocatalytic CO_2 reduction, although different possible reaction pathways are already identified based on analytical analyses using chromatographic methods, mass spectrometry, IR, EPR, theoretical studies and others.[79–84] Especially EPR is a very important tool since it is believed that radicals, which are paramagnetic due to the unpaired electron, play an important role as intermediates in the reaction pathway.

It is well known that CO_2 is a very stable, linear and inert molecule with $D_{\infty h}$ symmetry and a closed-shell configuration.[85] Since the carbon atom is considered electrophilic and the oxygen atoms both have free electron pairs, the molecular structure will bend after a single electron addition as a consequence of the electrostatic repulsion with the negatively charged carbon and oxygen atoms. This leads to a loss of symmetry and consequently a low electron affinity and high LUMO energy of the CO_2 molecule. Therefore, the reduction of CO_2 by one electron to an anion radical $CO_2^{\bullet-}$ has a negative potential of – 1.9 V versus normal hydrogen electrode (NHE).[86] This is highly unfavourable, making it almost impossible for any semiconductor to provide enough redox potential for this single electron reduction (Figure 7).

Proton-assisted multi-electron transfers are far more probable, such as two, four, six, and eight electron reductions (requiring the same number of protons) as shown in eqs. 4 – 9 to form respectively carbon monoxide, formic acid, formaldehyde, methanol, and methane. The electrochemical reduction potentials are similar to the one-electron reduction of a proton. In theory, these multi-electron reductions are feasible, as shown in Figure 7, but until now, evidence is still lacking. Most likely, the reduction proceeds via consecutive one-electron steps and therefore the main limiting step in CO_2 reduction remains the first electron transfer step.[1]

$$2H^+ + 2e^- \rightarrow H_2 \qquad E^0_{redox} = -0.41\ V \qquad \text{(eq. 4)}$$
$$CO_2 + 2H^+ + 2e^- \rightarrow CO + H_2O \qquad E^0_{redox} = -0.53\ V \qquad \text{(eq. 5)}$$
$$CO_2 + 2H^+ + 2e^- \rightarrow HCOOH \qquad E^0_{redox} = -0.61\ V \qquad \text{(eq. 6)}$$
$$CO_2 + 4H^+ + 4e^- \rightarrow HCHO + H_2O \qquad E^0_{redox} = -0.48\ V \qquad \text{(eq. 7)}$$
$$CO_2 + 6H^+ + 6e^- \rightarrow CH_3OH + H_2O \qquad E^0_{redox} = -0.38\ V \qquad \text{(eq. 8)}$$
$$CO_2 + 8H^+ + 8e^- \rightarrow CH_4 + 2H_2O \qquad E^0_{redox} = -0.24\ V \qquad \text{(eq. 9)}$$

CO_2 activation can be achieved with high efficiency using photocatalysts modified with noble metal nanoparticles. One of the pioneering works on this topic was published by Rasko *et al.* in which the bent anion radical $CO_2^{\bullet-}$ was formed on a Rh/TiO_2 catalyst as a consequence of the electron transfer from the d orbital of the Rh to the π* orbital (C-O).[81] Furthermore, Tanaka *et al.* studied the use of Pt co-catalysts in which the dissociation of CO_2 to CO was facilitated on the Pt sites.[87] Noble metal nanoparticles do not only catalyse the different CO_2 reduction steps, but they also play a major role in the selectivity towards a given end product.[87] It is important to notice that these reports involved noble metal nanoparticles that solely act as co-catalysts. Another parameter that merits attention, is specifically the type of light irradiation used in different reactors. This can have a direct impact on the adsorption/desorption/activation processes occurring at the photocatalyst surface, which in turn influence the CO_2 reduction pathway mechanism. It is known that the catalytic performance of metal NPs is directly correlated to the reaction temperature, while this is not generally valid for semiconductor photocatalysis. When CO_2 photoreduction is discussed, in many cases the plasmonic NPs are actively involved in surface reactions with the reactants or intermediates. Since the type of light irradiation can influence the temperature of the system, it is important to study this temperature effect in order to have a better

picture of the photocatalytic mechanisms.[88–90] In the following, the use of noble metal nanoparticles used for plasmonic enhancement will be highlighted in particular.

As such, the next part of the review is divided in three main sections organized based on product selectivity, with the focus on methane, carbon monoxide or methanol/ethanol as main products. Each of these sections starts with plasmonic nanostructures deposited on carbon-based supports and continues with plasmonic structures on inorganic supports.

4.2. Methane (CH₄) as main product

Methane represents the main component of natural gas and due to its continuous increasing demand, it is of the utmost importance to find an alternative solution for the long-term supply. Photocatalytic conversion of CO_2 has the potential to solve part of this problem through "solar methane". In the ideal case of "solar methane", the catalysed sunlight assisted photoreduction of CO_2 requires only water. If pure H_2 is used instead of water, the generated H_2 must originate from a green source.[91]

4.2.1. Carbon-based supports

Many studies report the use of Ag nanoparticles as plasmons because they are more cost-effective compared to other noble metals such as Au or Pt, and due to their strong plasmonic response. Abou Asi *et al.* used Ag/AgBr plasmonic deposited on a carbon based material support (CNT - carbon nanotubes) as photocatalysts to enhance the CO_2 reduction activity under visible light.[92] The photocatalyst in this study was AgBr, with an indirect band gap of 2.64 eV, thus in the visible range of the spectrum. Plasmonic Ag nanoparticles are formed when an excited electron (after light absorption) combines with an interstitial ion.[93–96] These photocatalytic systems, however, suffer from high electron-hole recombination rates, thus the authors proposed to deposit the photocatalyst material on carbon nanotubes in order to tackle this drawback. As a carbon based material support, CNTs have a high electron storage capacity and can act as an electron shuttle of which the Fermi level is -0.2 V vs. NHE.[97–101] Since the conduction band of AgBr has an energy of -1.04 eV vs. NHE, which is more negative than the band of CNT, electron transfer from Ag/AgBr to CNT will occur rapidly. In this way, the CNT can enhance the charge separation and offer increased stability to the Ag/AgBr photocatalyst. The experiments were performed in a pressurized stainless-steel vessel at 7.5 MPa. The photocatalyst powders were suspended in 0.2 M KHCO₃, through which pure CO_2 (99.99%) was bubbled for 30 min. Irradiation was done by a 150 W Xe lamp (25 mW cm⁻² at the irradiated surface) equipped with a 420 nm cut-off filter to ensure purely visible light irradiation. The study showed that depositing Ag/AgBr particles on CNTs had a significant impact on the CO_2 conversion rate, although the selectivity remained similar. Moreover, the longer the CNT chain, the higher the product yield. The detected products were CH₄, CH₃OH, CO, and CH₃CH₂OH of which the highest yield was obtained for CH₄ (30 μmol g_{cat}^{-1} h⁻¹).

Ong *et al.* used a slightly different approach by depositing halides (AgX) on protonated graphitic carbon nitride (g-C₃N₄), which resulted in heterostructured AgX/g-C₃N₄ (X = Cl and Br) nanocomposites able to achieve an exclusive selectivity towards CH₄.[102] A low-power 15 W energy-saving daylight lamp was used to irradiate the samples in a gas-phase photoreactor. The highest activity was achieved for 30% AgBr/g-C₃N₄ with a TOF towards

CH₄ of 1.3 μmol g_{cat}^{-1} h⁻¹. Methane appeared to be the only detectable product. This could be explained by the reduction potential of CO_2/CH₄ (-0.24 V) being lower than the reduction potentials of CO_2/CH₃OH (-0.38 V), CO_2/CO (-0.52 V), and CO_2/HCOOH (-0.61 V), leading to a preferential reduction of CO_2 to CH₄. The enhanced photoactivity was attributed to two synergistic effects: (1) SPR effect from Ag nanoparticles, formed upon light irradiation of AgBr deposited on g-C₃N₄, and (2) suppressed charge recombination due to the formation of a type II heterojunction between AgBr and g-C₃N₄, leading to an efficient charge transfer and separation. The latter was the main difference between AgBr/g-C₃N₄ and AgCl/g-C₃N₄ system as schematically shown in Figure 8. If g-C₃N₄ and AgX are illuminated, both will generate electron-hole pairs after which charge transfer will occur in the heterojunction by either Type I or Type II. The Ag/AgCl/g-C₃N₄ system proved to be a Type I heterojunction (Figure 8a), in which the valence band potential of AgCl was more positive and the conduction band potential of AgCl more negative than the respective bands of g-C₃N₄. This means that both the SPR-excited electrons in Ag and band gap excited electrons in AgCl were transferred to the conduction band of g-C₃N₄. Furthermore, also the band gap photogenerated holes of AgCl were transferred in the space charge region to g-C₃N₄, where they are consumed
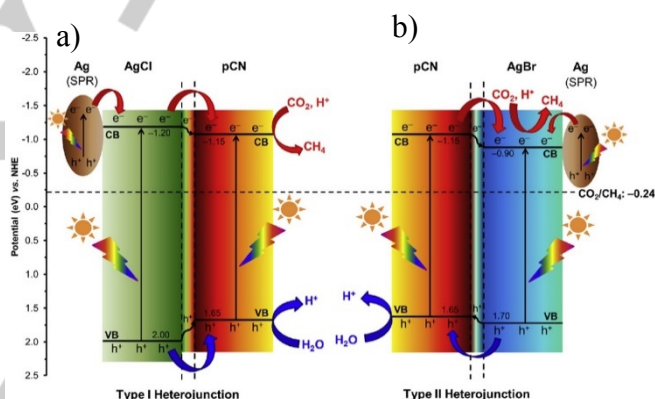
Figure 8. Schematic illustration of charge carrier transport in a) Ag/AgCl/g-C₃N₄, and b) Ag/AgBr/g-C₃N₄ heterojunctions for the photocatalytic CO_2 reduction. Reprinted with permission from ref.[102]

in the oxidation of H_2O to H⁺. Since both the electrons and holes are accumulated in g-C₃N₄, a higher rate of recombination occurs and thus a lower photocatalytic activity is obtained. On the contrary, Ag/AgBr/g-C₃N₄ forms a Type II heterojunction in which the electrons and holes are spatially separated and thus suppressing recombination. The SPR excited electrons in Ag as well as the band gap excited electrons in g-C₃N₄ are transported to the conduction band of AgBr. The holes, on the other hand, migrate from the valence band of AgBr to the valence band of g-C₃N₄, and are thus separated from the electrons. In this case, a synergistic effect between SPR and efficient charge separation has led to improved photocatalytic activity.

On the other hand, in a later study and following a different synthesis pathway, Murugesan *et al.* developed a plasmonic direct Z-scheme AgCl/g-C₃N₄ photocatalyst to reduce CO_2 in aqueous media under visible light illumination.[103] A classical direct Z-scheme photocatalyst consists of only two semiconductors that have direct contact at their interface. Specifically, a typical direct Z-scheme system has a charge-carrier migration pathway that resembles the letter "Z". During the photocatalytic reaction involving the Z-scheme mechanism (in

addition to the Type II mechanism), the photogenerated electrons from the CB of the semiconductor with lower reduction ability recombine with the photogenerated holes from the VB semiconductor with a higher oxidation ability than VB of the other semiconductor.[104,105]

A high selectivity of 89% towards CH_4 was obtained with a TOF of 6.6 µmol g_{cat}^{-1} h^{-1} due to a plasmonic effect as well as a reduction of charge recombination due to the Z-scheme. Taking into account the studies of Ong et al. and Murugesan et al., one can conclude that even for very similar materials, the photocatalytic reduction mechanism of CO_2 depends directly on the nano-architecture of the composite.[102,103]

In order to improve the photocatalytic properties of g-C_3N_4 as a support material for CO_2 reduction, Humayun et al. focused their work on phosphorus doped g-C_3N_4 decorated with Au nanoparticles. More specifically, they used a Au/P-doped g-C_3N_4 photocatalyst to enhance the CO_2 reduction towards CH_4, achieving a relatively high TOF of 24 µmol g_{cat}^{-1} h^{-1}.[106] They have shown that due to the P doping and the deposition of the Au nanoparticles, more visible light could be absorbed (by reducing the band gap energy of g-C_3N_4 from 2.7 eV to 2.38 eV for P-g-C_3N_4) and a better charge separation was obtained due to the dopant induced surface states and the Au nanoparticles. The plasmonic near-field effect of Au further enhanced the activity.

4.2.2. Inorganic supports

Besides the carbon-based supports, a series of studies report remarkable results for CH_4 production using inorganic supports in tandem with plasmon nanoparticles. He et al. synthesized Ag/$AgIO_3$ particles to achieve high selectivity towards CH_4 with a TOF of ca. 6 µmol g_{cat}^{-1} h^{-1}.[107] They assumed that the driving force of the photocatalytic reduction arises from the shift of the Fermi level of $AgIO_3$, caused by the effect of the surrounding medium (Ag nanoparticles). The experiments were performed under purely visible light using a 500 W Xe lamp equipped with a 400 nm cut-off filter. In a later study, Wang et al. managed to achieve 70% selectivity towards CH_4 using a similar type of catalyst, namely Ag-supported nanoparticles on an inorganic Ag-based support, Ag_2SO_3.[108] They synthesized Ag/Ag_2SO_3 via an ion-exchange method with subsequent reduction using hydrazine hydrate. Under purely visible light irradiation, they achieved the reduction of CO_2 towards CH_4 at 3 µmol g_{cat}^{-1} h^{-1}, and 1.24 µmol g_{cat}^{-1} h^{-1} towards CO with a 5% Ag/Ag_2SO_3 catalyst. Contrary to He et al., the authors assumed that the main mechanism for the enhanced activity was the SPR induced electron injection from the Ag nanoparticles to the Ag_2SO_3 photocatalyst and not the shift of the Fermi level of the supporting material ($AgIO_3$) caused by Ag plasmons.[107] In order to explain the selectivity, they assumed that from all possible reaction products, CH_4 (CO_2/CH_4 -0.24 V vs. NHE), CH_3OH (CO_2/CH_3OH -0.38 V vs. NHE), CO (CO_2/CO -0.53 V vs. NHE), and HCOOH ($CO_2/HCOOH$ -0.61 V vs. NHE) will mainly be formed.[109] Under complete thermodynamic control, the product yield for CO_2 reduction is expected in the order: CH_4 > CH_3OH > CO > HCOOH. Under kinetic control on the other hand, the product yield towards CO would be higher than towards CH_4, because only two electrons are needed for the reduction towards CO, whereas towards methane is an 8 electron reduction. Since in this study only CH_4 and CO were formed (with a higher selectivity towards CH_4) it is assumed that both thermodynamics

as well as kinetics play an important role in the plasmonic CO_2 reduction with water vapor.

Zhao J. et al. used 3D porous ZnO nanosheets as semiconductor and modified them with three different plasmonic nanoparticles: Au, Ag (see 4.3) and Pd.[110] They found that different products were obtained by changing the plasmonic metal, possibly correlated with the strong influence of the metal-semiconductor interaction, which modifies the CO_2 photoreduction pathway. Moreover, the specific selectivity for separate products of each plasmon metal was confirmed by DFT calculations. The photocatalytic tests, performed under solar light irradiation, showed that the use of Pd leads to the formation of CH_4, with a selectivity of 85% and a TOF of 18 µmol g_{cat}^{-1} h^{-1}. Moreover, Blommaerts et al. observed a similar change in product selectivity when studying Pd and Pt plasmonic particles deposited on Ti-Beta zeolites.[111] More specifically, an inversion of selectivity towards CH_4 resulted when Pd was used on Ti-Beta zeolite, compared to bare Ti-Beta zeolite and the Pt/Ti-Beta zeolite system (see 4.3).

TiO₂-based support

As the most studied material in photocatalysis, TiO_2 is reported in a series of scientific papers as efficient inorganic support for CO_2 to CH_4 reduction when used in the same nanoarchitectures with plasmon nanoparticles. Feng et al. used double-shelled plasmonic Ag/TiO_2 hollow spheres for the visible light reduction of CO_2 into CH_4.[112] The reactions were performed using a 300 W Xe lamp (420 nm cut-off filter) to achieve a TOF for methane of 1.6 µmol g_{cat}^{-1} h^{-1}. They attributed that high enhancement in comparison with bare TiO_2 to three distinct mechanisms. First of all, the SPR of Ag nanoparticles managed to harvest more (visible) light with subsequent charge transfer from Ag to TiO_2. Secondly, photons are trapped in the hollow structure which leads to scattering events and therefore an enhanced light absorption. Lastly, the Ag/TiO_2 hollow spheres offer a relatively high surface area of 61 m²/g.

Yu et al. carried out the reduction reaction both in gas phase and in aqueous phase, using a similar system as Feng et al. (Ag/TiO_2), to study the effect of the medium on the product selectivity.[112,113] Both reactions were carried out using a 300 W Xe lamp. For pristine TiO_2 in gas phase, the main product that was formed was CH_4 at a rate of 0.61 µmol g_{cat}^{-1} h^{-1}. The addition of 1.5 wt% Ag led to an increase in TOF for CH_4 to 1.4 µmol g_{cat}^{-1} h^{-1} which could be attributed to the combined effect of SPR and electron sink properties of Ag. In the aqueous phase, on the other hand, the main product was CH_3OH at a TOF of 4.2 µmol g_{cat}^{-1} h^{-1} (besides small amounts of CH_3COCH_3 and CH_3CHO). The silver loading ranging from 1 wt% to 2 wt% did not influence the results significantly, whereas in the gas phase 1.5 wt% silver loading was identified as the optimum. The authors proposed that this difference in selectivity depending on the gaseous versus aqueous reaction medium could be attributed to different reaction mechanisms. In the gas phase, a number of fast deoxygenation processes occurs for CO_2, in which the oxidation state of carbon decreases from +IV (CO_2) to +II (CO), 0 (C•), -I (CH•), and finally -III (CH_3•). The last step is combining a H• radical with the CH_3• radical with the formation of CH_4. In the aqueous phase, on the other hand, there is a large excess of H_2O molecules leading to a number of fast hydrogenation processes for CO_2. Here, the oxidation state of carbon decreases from +IV (CO_2) to +II (HCOOH), 0 (HCHO), to the final state -II (CH_3OH). The formation

of other end products such as CH_3COCH_3 and CH_3CHO is a consequence of coupling reactions of intermediate radicals.

Dilla *et al.* deposited both Ag and Au on a TiO_2 P25 material and found that the highest activity towards CH_4 was achieved with a Ag/TiO_2 sample.[114] The difference between Au and Ag is mainly attributed to a better overlap between the absorption spectrum of P25 and the plasmon band of Ag in comparison with Au. This enables the near-field mechanism to transfer energy to the photocatalyst in the case of Ag and not in the case of Au, even though the direct electron injection mechanism should be present in both cases. Even if the results for Au/P25 were slightly lower than the ones for Ag/P25, the comparison provided unique information on possible ways to increase the photocatalytic activity by improving the overlap of the plasmon absorption nanoparticles and the semiconductor band gap energy. In the same line Asapu *et al.* proved the dominant role of the near-field mechanism over direct electron transfer mechanism through a series of theoretical simulations, surface enhanced Raman spectroscopy (SERS) experiments and photocatalytic tests.[75]

In a more complex study, Low *et al.* confirmed the importance of the near-field effect on the photocatalytic process involving TiO_2 and Ag plasmons.[115] More specifically, the authors aimed at directly unravelling the plasmonic effect that formed the basis for enhanced CO_2 reduction to CH_4 with Ag-loaded TiO_2 nanotube arrays (TNTAs). In first instance, they designed an experiment to distinguish between the hot electron injection mechanism and enhanced charge separation due to the Schottky barrier between Ag and TiO_2. Using Synchronous-illumination X-ray photoelectron spectroscopy (SIXPS), they observed two peaks around 458.8 and 464.8 eV characteristic for Ti $2P_{3/2}$ and Ti $2p_{1/2}$ core levels. In dark conditions, the Ti $2P_{3/2}$ peak shifted positive after the addition of Ag nanoparticles, due to an electron density decrease in the TNTAs. This is because after the formation of the Schottky barrier, electrons in the TNTAs migrate towards the Ag nanoparticles to align the fermi level energies. Under illumination, the pristine TNTAs showed no shift in the SIXPS spectrum, while in the case of Ag/TNTAs a negative shift was observed for the Ti $2P_{3/2}$ peak. This indicates an increase in electron density on the TNTA surface. This means that due to the SPR effect, hot electrons are generated in the Ag nanoparticles with enough energy to overcome the Schottky barrier to transfer towards the TiO_2 surface. Furthermore, the authors proved that not only the hot electron injection mechanism is important. They used electrochemical impedance spectroscopy (EIS) to investigate the charge carrier transport performance. The results suggested that by depositing Ag onto the TNTAs, charge carrier transport can be improved. This could be attributed to an enhanced near-field effect of the Ag SPR. To support this hypothesis, finite-difference time-domain (FDTD) methods were used to simulate the field distribution of the TNTAs. They observed local hot spots of intense electric near-field, especially if the Ag nanoparticles were deposited on the inside of the TiO_2 nanotubes.

A comprehensive study by Collado *et al.* attempted to clarify the specifics involved in the photoreduction of CO_2, followed by a combination of theoretical calculations, advanced *in-situ* and time-resolved methods.[116] For this, the authors used Ag nanoparticles deposited on anatase TiO_2 to unravel the effect of charge dynamics at the plasmonic metal/semiconductor interface. Under UV light illumination by four 6 W lamps (365 nm) they obtained a high selectivity towards CH_4 and a 15-fold increase in CH_4 evolution (5.8 µmol g_{cat}^{-1} h^{-1}) by using Ag/TiO_2 in comparison

with pristine TiO_2. Under visible light, on the other hand, a high selectivity towards CH_3OH was observed. In first instance, they showed that the density of states (DOS) of pristine TiO_2 shows a band gap of 3.2 eV, in which O 2p orbitals form the valence band and Ti 3d orbitals the conduction band. By modifying TiO_2 with Ag nanoparticles, induced interface states are formed in the band gap of TiO_2 due to the donation of charge from Ag 5s to O 2p neighbouring atoms and Ti 3d orbitals. These surface sub-band gap states have already been described and are consistent with ultrafast (< 10 fs) hot electrons generated in TiO_2 instead of transferred electrons from Ag, which could play an important role in the activity under visible light.[117] Furthermore, by using *in-situ* near-ambient pressure XPS (NAP-XPS) a mechanistic study on the CO_2 photoreduction was performed. The first step under dark conditions included the adsorption of CO_2 in which carbonate/bicarbonate is formed in first instance and afterwards preferential hydrocarbon intermediates. Different signals were observed of which the C1s signal of Ag/TiO_2 shows spurious carbon (C-C, 284.7 eV), HCO_3^- (288.6 eV), CO_3^{2-} (289.5 eV) and species containing C-O bonds (285.5 eV).[117–119] In the O 1s region, bridge oxygen species (O_B, 530.1 eV), hydroxyl groups (O_{OH}, 531.1 eV), inorganic C-O• species (532.0 eV) and physisorbed water (532.5 eV) could be detected.[120,121] Irradiating the samples with UV light clearly changed the components found in the spectra. In the C1s spectrum new components were detected: methylene (284.0 eV) and formate (287.0 eV) intermediates and $CO_2^{\delta-}$ (291.9 eV) and desorbed CO_2 (292.9 eV).[122–124] The already present peaks of HCO_3^- and CO_3^{2-} were broadened and could act as hole scavengers components.[125] Different carbonyl intermediates were assigned to the 287.01 eV peak.[118,126] Finally, in the O1s spectrum, a decrease is observed in OH groups and physisorbed water. This means that both species play an important role in the photoredox process during the reaction.

Hong *et al.* synthesized Ag nanoparticle cores encapsulated by a TiO_2 shell using a hydrothermal method to achieve a high selectivity towards CH_4 at a TOF of 5 µmol g_{cat}^{-1} h^{-1}, which was a 10-fold activity increase compared to pristine TiO_2 nanoparticles.[127] This large increase was attributed to a band gap improvement of the TiO_2 shell as a consequence of the Ag core and an increase of photon flux induced by the plasmonic Ag core, mainly due to the light scattering effect. Moreover, when the light source was restricted to wavelengths higher than 400 nm, a considerably lower amount of CH_4 was formed. These results are in good agreement with the observations of Collado *et al.*, highlighting the importance of the UV light for a decent CH_4 formation.[116]

Next to Ag, Au is one of the most commonly used plasmonic metals due to its higher stability (especially compared to silver) and a good activity enhancement. More specifically, besides Ag/TiO_2 systems, Au/TiO_2 represents one of the most studied nanocomposites when discussing fundamental photocatalysis, using plasmons coupled with semiconductor materials. The first reference on CO_2 conversion, that can be tracked, dates back to 2011 in which Hou *et al.* used Au nanoparticles deposited on top of a TiO_2 film.[128] A TiO_2 thin film consisting purely of anatase was prepared by a sol-gel method and deposited on a glass/quartz substrate by spin coating to achieve a 400 nm thick film. The Au nanoparticles are deposited on top of the TiO_2 film by electron beam evaporation under vacuum to create a 5 nm thick gold film. This layer was not thick enough to ensure the formation of a

continuous film, but it rather formed different islands, regarded in this work as nanoparticles. The CO_2 reduction reaction was carried out using CO_2 saturated water vapor under either UVC/UVA light illumination (254 nm, 20 mW cm^{-2}; 365 nm, 20 mW cm^{-2}) or purely visible green laser light (532 nm, 350 mW cm^{-2}) for 15 h at slightly elevated temperature (75°C). Under purely visible light, only CH_4 was formed with a product yield of 1.5 µmol m_{cat}^{-2} h^{-1}. The enhancement for the Au/TiO₂ system in comparison with bare TiO₂ under 532 nm illumination was attributed to the intense near-field of the Au nanoparticles coupled to the short-lived defect state absorbance of TiO₂. Under UVC illumination (254 nm), only CH_4 was formed in the case of TiO₂ (16.7 µmol m_{cat}^{-2} h^{-1}) but other products such as ethane, formaldehyde, and CH_3OH were formed for the Au/TiO₂ system. This could be explained by the fact that the conduction band of bare TiO₂ lies below the reduction potentials of CO_2/HCHO and CO_2/CH_3OH but above CO_2/CH_4. This means that only CH_4 can be formed. For Au, at 254 nm illumination (corresponding with an energy of 4.88 eV) interband transition occurs from the d-band to the conduction band above the reduction potentials of CO_2/HCHO, CO_2/CH_3OH, and CO_2/CH_4. Under 365 nm UV light illumination, again only CH_4 was formed, both for TiO₂ (1.2 µmol m_{cat}^{-2} h^{-1}) as for Au/TiO₂ (1.3 µmol m_{cat}^{-2} h^{-1}).

Wang R. *et al*. used gold nanoparticles to modify TiO₂ nanosheets in their so-called 0D/2D composite system, to obtain a high TOF towards CH_4 of 70 µmol g_{cat}^{-1} h^{-1} with a selectivity of around 80%.[129] This was valid for the experiments performed under Xe arc lamp (300 W) irradiation, while the monochromatic 550 nm assisted experiments led to the formation of only CO. The findings strengthen the idea that multi-electron reactions to obtain CH_4 or CH_3OH by the photoreduction of CO_2 in the presence of Au/TiO₂ require the assistance of UV light.

Khatun *et al*. used an electrochemical deposition method to synthesize Au decorated TiO₂ nanotube arrays for efficient reduction of CO_2 to CH_4 under visible light irradiation.[130] In this way, a doubling in CH_4 production was obtained in comparison with bare TiO₂ nanotube arrays. Both, a plasmonic effect as well as an improved charge separation effect, evidenced by photoluminescence analysis, lay on the basis of this improved activity. In the case of Khatun *et al*. and Wang *et al*., the light source (Xe arc lamp, 300 W) and the photocatalyst composition (Au/TiO₂) are very similar.[129,130] However, it is very challenging to compare the CO_2-to-CH_4 conversion results measured in these two studies, due to the distinctive way of reporting the CH_4 formation yield. Thus, it would represent a step forward if the scientific literature would report the results in a more standardized manner. Zeng *et al*. assembled an unconventional Au-TiO₂ system by the use of TiO₂ nanotube arrays with periodically modulated diameters as photonic crystals on which Au plasmon nanoparticles were deposited.[131] The nanoarchitecture consisting of plasmonic photonic crystals (Au-PMTiNTs) achieved an impressive 302 µmol g_{cat}^{-1} h^{-1} production rate of CH_4 under simulated sunlight (Figure 9). The authors base their explanation for the high selectivity towards CH_4 (~ 90%) on the presence of the photonic crystals which in turn have a so-called photonic band gap (PBGs). These PBGs of PMTiNTs act as a filter for specific wavelengths, blocking the defect mediated low energy transitions which may increase the chance for the formation of other products. As a result of sufficient e⁻ transition to the CB of TiO₂ and filtering-like properties of PMTiNTs (through PBG), Zeng *et al*. assume the

"carbene" pathway as the main route for the CO_2/CH_4 formation, since it is more thermodynamically feasible than CO_2/CO:
$$CO_2 \xrightarrow{e^-} \cdot CO_2^- \xrightarrow{H\cdot} CO + OH^- \xrightarrow{e^-} \cdot CO^- \xrightarrow{H\cdot} C \cdot + OH^- \xrightarrow{H\cdot} \cdot CH \cdot$$
$$\rightarrow CH_2 \cdot \rightarrow \cdot CH_3 \rightarrow CH_4 - \text{"Carbene" pathway.}[131]$$

Deposition of bi-metallic plasmonic nanoparticles represents a versatile method to boost the activity of the classic TiO₂ support in photocatalysis. In a recent study, Ziarati *et al*. constructed hierarchical yolk@TiO₂-xHx particles modified with core@shell bi-metallic Au@Pd plasmonic nanoparticles to achieve a TOF towards CH_4 of 47 µmol g_{cat}^{-1} h^{-1}.[132] The main factors for improved activity were a high gas adsorption, intense electron transportation and high visible light activation. Here, it is important to highlight that the visible light activation was achieved due to the presence of Au in the photocatalyst and not related with the presence of Pd, which has the LSPR absorption in the UV range.[30] The authors suggest that the hot electrons of Au NPs
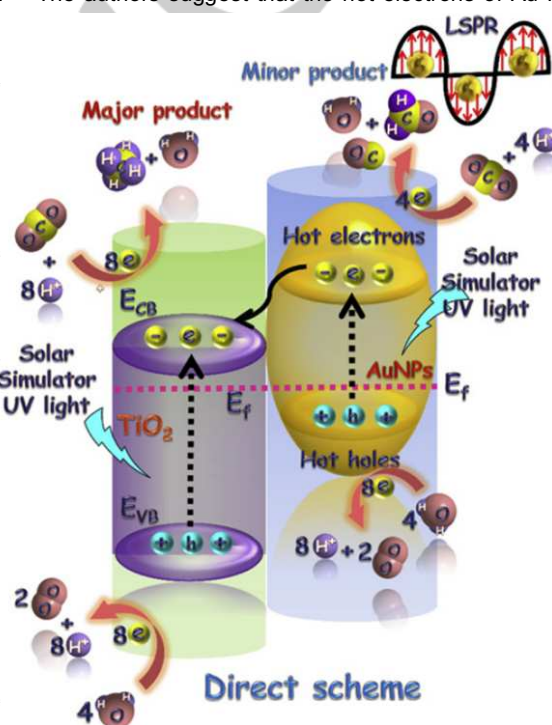
Figure 9. The formation of CH_4 in the presence of Au-PMTiNT system and under AM1.5 G solar illumination. Reprinted with permission from ref.[131]

are injected into the Pd shell and as a result of this electron transfer, the CO_2 photoreduction towards CH_4 increased. At the same time, according to Ma *et al*., Pd can also form Pd-H species (by decomposing the H₂O), and together with the CO• radicals adsorbed on Pd further form •C radicals able to combine with •H radicals successively, to result in •CH, •CH₂, •CH₃, and finally CH_4.[133]

Another possible way to improve the photoreduction of CO_2 towards CH_4 by the already promising Ag/TiO₂ and Au/TiO₂ materials is to introduce another semiconductor, creating two extra heterojunctions in the system. Zhang *et al*. used a complex hetero-nano-structured photocatalyst consisting of plasmonic nanoparticles, ZnIn₂S₄ nanosheets, and TiO₂ nanofibers (Au/ZnIn₂S₄/TiO₂ or Ag/ZnIn₂S₄/TiO₂), to use the heterojunction effect, SPR-coupling, and structural advantage in order to obtain a large electron transfer rate constant.[134] The Ag/ZnIn₂S₄/TiO₂ system showed a 16-fold enhancement of the CO_2 reduction activity in comparison with bare ZnIn₂S₄ nanosheets. The

11

catalysts were irradiated for four hours with a 300 W Xe lamp (280 nm < λ < 780 nm) in order to optimize the CH_4 yield. They achieved a high CH_4 production of 6290 ppm g_{cat}^{-1} h^{-1}. A distinct approach was followed by Jiang *et al.* which led to the development of $Au/TiO_2/W_{18}O_{49}$ sandwich-like structures.[135] The reasoning for the remarkable photocatalytic reduction of CO_2 towards mostly CH_4 (selectivity 93.3%) was correlated not only to the good light harvest and implicit the formation of "hot electrons" with extended lifetime, but also due to the Au-O-Ti and W-O-Ti active sites. Based on practical experiments and modelling, the authors were able to suggest that the dual-hetero-active-sites (Au-O-Ti, W-O-Ti) captured protons and CO intermediates at the interface of $Au/TiO_2/W_{18}O_{49}$, synergistically enhancing the CO_2 photoreduction. The mechanism involving the plasmon-coupling-induced hot electron generation and transfer between $Au-W_{18}O_{49}$ to TiO_2 is shown in Figure **10**. Using H_2O as hydrogen source, they achieved productions rate of 35.55 μmol g_{cat}^{-1} h^{-1} CH_4 and 2.57 μmol g_{cat}^{-1} h^{-1} CO under vis-NIR light irradiation (λ > 420 nm, approx. 50 mW/cm^2).
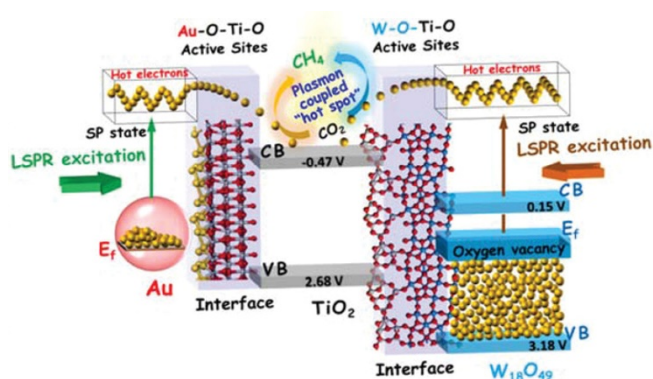
Figure 10. Mechanistic illustration of the photocatalytic reduction of CO_2 into CH_4 via the dual-hetero-interface (sites) of $Au-W_{18}O_{49}-TiO_2$. Reprinted with permission from ref.[135]

Bian *et al.* designed a 3 components nanocomposite consisting of plasmonic gold nanorods (1D material) deposited on TiO_2 nanosheets (2D) and $BiVO_4$ nanoflakes (2D).[136] They achieved a high enhancement in photocatalytic activity towards CH_4 with a TOF of 16.25 μmol g_{cat}^{-1} h^{-1}. This was attributed to the increased surface area due to the 2D $BiVO_4$ nanoflakes, the coupling of the TiO_2 nanosheets with the $BiVO_4$ nanoflakes that serve as energy platform to accept electrons from $BiVO_4$, and the plasmonic enhancement due to the Au nanorods with simultaneous enhanced charge separation.

In addition to relatively simple systems involving one type of plasmonic nanoparticle and one or two semiconductors, one can build many other types of nanoarchitectures in order to benefit from the positive effect of the plasmons for the CO_2 photoreduction. Keeping this in mind, Bera *et al.* used a Pt/TiO_2 photocatalyst, in which the Pt acts as a co-catalyst, modified with plasmonic Au and $Au@SiO_2$ core-shell nanoparticles.[137] They used LED illumination with two different wavelengths, 365 nm and 530 nm. It was shown that under purely 365 nm illumination, no influence on the CH_4 evolution could be observed by using Au or $Au@SiO_2$ nanoparticles. Under both 365 nm and 530 nm illumination, however, the photocatalytic activity was clearly increased due to the SPR effect of Au triggered by the 530 nm LED. The highest activity was found for 18 nm Au nanoparticles,

as it was proven that the SPR intensity increases with the growth of the plasmonic NP size from 4 to 18 nm. In the case of $Au18@SiO_2$ core-shell the increase was 3.1 times higher compared to the pristine Pt/TiO_2, to reach a TOF for CH_4 of 2.98 μmol g_{cat}^{-1} h^{-1}. First of all, due to the SPR of Au, more electron-hole pairs are generated in the TiO_2 photocatalyst because of the near-field enhancement. Moreover, the authors report that local heating had a contributing effect on the activity. And lastly, also hot electron injection from Au to TiO_2 occurs in this system. These electrons can then in turn be transferred to the Pt co-catalyst, which serves as electron sink to enhance charge separation. By coating the Au nanoparticles with a SiO_2 shell, the dielectric environment changes around the nanoparticles and therefore also the SPR properties. It has been shown in other research that coating of a passivation layer such as SiO_2 or Al_2O_3 can enhance the SPR of Au.[23,70] The consequence of coating with an insulating layer, is that the hot electron injection mechanism is suppressed, but the electric near-field is enhanced even more in the case of the $Au@SiO_2$ core-shell nanoparticles and thus will be the dominant mechanism for enhancement in this system. Mankidy *et al.* used TiO_2 modified with Ag, $Ag@SiO_2$ core-shell, Pt, and Ag-Pt bimetallic nanoparticles to increase the rate of electron production and simultaneously minimizing the electron losses.[138] This can be achieved by improved electron-hole pair generation, electron trapping on the surface, electron accumulation, or increased electron transfer from semiconductor to CO_2. To perform the experiments, a batch reactor was used in which 1 g of photocatalyst material was loaded. A CO_2 stream bubbled through H_2O was fed to the reactor after which the system was pressurized to 10 psi and illuminated by a 100 W Hg lamp. They concluded that the use of $Ag@SiO_2$ nanoparticles increased the formation of electron-hole pairs by a plasmonic effect whereas the different bare metals (Ag, Pt, and Ag-Pt bimetallic) acted merely as co-catalysts to enhance the selectivity towards CH_4. It was shown that Pt greatly enhances the selectivity towards CH_4. Moreover, the combination of $Ag@SiO_2$ and Pt nanoparticles on TiO_2 led to an 8-fold increase in total electronic yield compared to bare TiO_2, however, the highest selectivity towards CH_4 was achieved when $Ag@SiO_2$ was used in combination with Ag-Pt bimetallic nanoparticles. The reason for this being related with the advantages provided by the presence of both plasmons in the bimetallic catalyst. More specific, silver having a high electron accumulation capacity, while Pt having a quick electron traversing behaviour. Similar to the case of Ziarati *et al.*, the presence of Pt is not so much correlated with the light absorption activity (same as for Pd the LSPR absorption is in the UV range), but with the fast transfer of the photogenerated electrons to the CO_2 molecules.[30,132]

The findings regarding the importance of the near-field effect in photocatalytic reactions are in good agreement with the data reported by Asapu *et al.*, Dilla *et al.* and Bera *et al.*. Moreover, the studies of Bera *et al.* and Mankidy *et al.* prove that a SiO_2 dielectric medium around the plasmon nanoparticles enhances the Au/Ag LSPR effect.[75,114,137,138]

Finally, next to commonly used noble metals such as Au and Ag, a series of other metal nanoparticles can show interesting plasmonic behaviour. Especially more cost-effective metal nanoparticles such as Cu are gaining more and more attention. Tan *et al.* used plasmonic Cu nanoparticles deposited on TiO_2 nanorods to achieve a high selectivity towards CH_4.[139] The experiment was performed in a flat bottom stainless steel reactor,

equipped with a quartz window on top, illuminated by four UVA lamps (365 nm, 3.25 mW cm^{-2}). Water was used as reaction medium, saturated with ultrapure CO_2. A CH_4 yield of 2.91 ppm g_{cat}^{-1} h^{-1} was achieved, which outperformed both the bare TiO_2 nanorods as well as a TiO_2 P25 reference material. It should be noted here that the authors believe that a separation of electrons and holes is the main mechanism for the enhanced activity, and only a mild LSPR effect is expected, due to the instability of Cu nanoparticles in air. Lee *et al*. modified porous TiO_2 with plasmonic columnar Cu nanostructures of tunable length.[140] These types of nanostructures led to a high enhancement of the CH_4 production rate upon the photocatalytic degradation of CO_2 under AM1.5 illumination. The highest activity was achieved for columns with a length > 160 nm, reaching a TOF of 124.3 ppm g_{cat}^{-1} h^{-1}. Contrary to Tan *et al*., the authors concluded that the main reason for the enhanced CH_4 production is due to the plasmonic effect of Cu nanoparticles (direct electron transfer mechanism), while the reflective characteristic of Cu contributes to a much lesser extent to the total photocatalytic process.[139] At the same time, both studies report as a drawback the reduced stability of the Cu nanoparticles under the photoreduction conditions, thus a stabilization of the Cu plasmons would be valuable in order to improve these types of catalysts.

4.3. Carbon monoxide (CO) as main product

Carbon monoxide is a valuable building block component in industrial applications as feedstock for the production of a wide variety of fuels, fertilizers, solvents *etc*. In many industrial processes, CO is used in combination with H_2 as "syngas".[141]

For the photoreduction of CO_2 towards CO a series of studies report the use of g-C_3N_4 as support for plasmonic nanoparticles. Li *et al*. have modified g-C_3N_4 with Au to shift the selectivity from CO to CH_4.[142] With pristine g-C_3N_4, however, a high selectivity towards CO (of 97%) was achieved, with a TOF of 5.2 μmol g_{cat}^{-1} h^{-1}. By depositing Au on the photocatalyst, an increase in photocatalytic activity was observed, leading to a TOF towards CO of 6.6 μmol g_{cat}^{-1} h^{-1}. The selectivity, on the other hand, slightly shifted to CH_4 to reach 81% CO and 19% CH_4 and a TOF towards CH_4 of 1.55 μmol g_{cat}^{-1} h^{-1}. Both hot electron injection and enhanced charge separation were the basis for this improved photocatalytic activity.

Next, Li *et al*. tested the photoreduction capabilities of CO_2 for a system consisting of the same elements as Li *et al*.[142,143] Specifically, the authors altered g-C_3N_4 with Au to achieve a selectivity of 68% towards CO with a TOF of 10 μmol g_{cat}^{-1} h^{-1}. Furthermore, they investigated the effect of the size of the Au nanoparticles on the activity. Using FDTD simulations, it was found that by increasing the size of the Au nanoparticles, a stronger SPR effect could be achieved, as was also confirmed by the study of Bera *et al*. (see 4.2).[137] The stronger SPR was correlated with the higher number of hot electrons that can be transferred from the nanoparticles to g-C_3N_4. On the other hand, smaller nanoparticles have a better separation efficiency of electron-hole pairs and thus reduced recombination. One can conclude that two seemingly contrasting approaches may both improve the SPR effect of the plasmons: (i) the use of an "ideal" very narrow particle size distribution or (ii) the use of various particles sizes in order to gain a synergistic effect.

Recently, Li F. *et al*. modified amine-functionalized g-C_3N_4 with Au nanoparticles to achieve a 7.6 times higher TOF towards CO

(28 μmol g_{cat}^{-1} h^{-1}) in comparison with pristine g-C_3N_4.[144] Three different factors explained this high increase in activity: (i) an improved adsorption capacity for CO_2 due to the amino group functionalization, (ii) energy transfer and temperature increase due to hot electrons generated in the gold nanoparticles, and (iii) improved charge separation due to the Schottky junction between Au and g-C_3N_4. In addition to electron injection and efficient charge separation of Au/g-C_3N_4 reported by Li *et al*. and Li *et al*., the system developed by Li *et al*. provides enhanced CO_2 adsorption, thus the latter photocatalyst may be regarded as superior.[142–144]

Similar to the photoreduction of CO_2 to CH_4, the inorganic supports play a very important role in the CO formation mechanism. Wan *et al*. used Ag/$SrTiO_3$ to selectively reduce CO_2 to CO with a TON of 80 μmol g_{cat}^{-1}.[145] The authors suggest that the reasons behind the CO_2 photoreduction are related to the enhanced visible light absorption induced by the Ag plasmons LSPR and the improved charge separation and transfer at the metal-semiconductor interface. Unfortunately, the total reaction time was not mentioned. Following a series of experiments on Au decorated ZrO_2 catalysts in the presence of solar and visible light irradiation, Gu *et al*. reached a similar conclusion for the enhanced activity of Au/ZrO_2 compared to the bare support.[146] They obtained a 25.6 μmol g_{cat}^{-1} h^{-1} formation rate for CO and 5.1 μmol g_{cat}^{-1} h^{-1} formation rate for CH_4 under solar light illumination. Due to the high band gap energy of ZrO_2 (5.3 eV), the visible light (λ > 420 nm) is not able to activate the catalyst, thus the authors assume that the hot electrons transferred from Au to the CB of ZrO_2 assist in the reduction of CO_2 at the surface of ZrO_2. Contrary to Zeng *et al*., where the suggested "carbene" pathway (see 4.2) led to the formation of CH_4, the majority product formed here, following the same route was CO.[131] As similar light irradiation and Au plasmons were deposited in both cases, one possible explanation for the very different selectivity may be related with the completely different properties of the supporting material, but such hypothesis would need to be confirmed experimentally. Recently, Liao *et al*. provided insights on the photocatalytic mechanisms able to reduce CO_2 in the presence of a perovskite-type $CsPbBr_3$ and Au nanocrystals.[147] The experiments performed under two different light wavelengths (λ > 420 nm and λ > 580 nm) showed two possible mechanisms. When the higher wavelengths (λ > 580 nm) was selected, only the Au NPs were photo-responsive. As a consequence, the authors suggest that for the $CsPbBr_3$-Au nanocomposite the Au LSPR-induced hot elections were transferred to the CB of $CsPbBr_3$ and participated in the CO_2 photoreduction. These findings are similar with the ones of Wan *et al*. and Gu *et al*.[145,146] However, when the lower wavelength (λ > 420 nm) was employed, the photogenerated electrons are coexisting in both materials and according to thermodynamically favourable principle, the electrons are displaced into Au, sustaining the CO_2 reduction reactions. In this case, the highest photoreduction yield towards mostly CO was observed, with a 3.2 folds enhancement when compared to pure $CsPbBr_3$.

Besides Pd (see 4.2) plasmonic nanoparticles deposited on porous ZnO, Zhao J. *et al*. investigated also the Ag/ZnO and Au/ZnO systems.[110] When Ag was used, a selectivity of 85% towards CO was obtained, with a TOF of 25 μmol g_{cat}^{-1} h^{-1}. It is important to notice that bare 3D porous ZnO nanosheets already showed a high selectivity (79%) towards CO with a TOF of 4 μmol g_{cat}^{-1} h^{-1}. Moreover, for ZnO loaded with plasmonic Au

nanoparticles, the highest activity was found for 4.6 mol% Au with a TOF of 27 µmol g_{cat}^{-1} h^{-1} towards C_2H_6, and a selectivity of 58%. Wang *et al*. also used a ZnO catalyst, modified with 20 nm Au nanoparticles under laser illumination (532 nm) to study the effect of local heating on the selectivity towards CH_4 or CO.[67] In the experiment, they used a gas mixture of 25% CO_2 and 75% H_2. Two different methods of laser illumination were chosen: (i) a continuous wave method (intensity ~ 10^4 W m^{-2}) or (ii) a 5.5 ns pulsed laser (peak intensity ~ 10^{12} W m^{-2}). They have shown that local temperatures of 600°C could be achieved at a laser intensity of 8 x 10^5 W m^{-2}. The interesting part of this research was that at low laser intensities, and thus low temperatures, a high selectivity towards CH_4 was observed whereas at high temperatures, mainly CO was formed. The authors hypothesized that the reaction pathway was a combination of two important chemical reactions, the reverse water-gas shift (RWGS) and CO methanation reaction:

$CO_2 + H_2 \rightleftharpoons CO + H_2O$ (RWGS)

$CO + 3H_2 \rightleftharpoons CH_4 + H_2O$ (CO methanation)
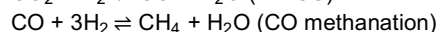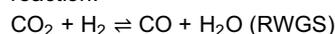
At the same time, Wang *et al*. suggest that in their case, the CO_2 photoreduction is a thermally-driven reaction and other contributions are absent or negligible.[67] It is important to mention that the experimental results follow the same trend as simulated values for the equilibrium composition of RWGS and CO methanation, although crossover of selectivity happens at lower temperatures in the experiments. This is due to highly localized heating (higher than the temperature measured of the Au-ZnO sample) close to the Au nanoparticles.

Robatjazi *et al*. focused their efforts on cheaper alternative materials able to photoreduce CO_2.[148] They synthesized Al nanocubes deposited on Cu_2O for which they measured a high increase in CO formation rate, especially at very high visible light intensities, up to 10 W cm^{-2}. The observations suggest a different photoreduction mechanism than the one of Wang C. *et al*., even if similar elevated local temperatures were involved in the process.[67] Through a series of experimental studies backed by theoretical models, the authors proved the dominant role of the photogenerated carriers, and not the photothermal heating effect, in CO formation.

Kawamura *et al*. used $[Zn_3Ga(OH)_8]_2CO_3 \cdot mH_2O$ layered double hydroxide (LDH) modified with plasmonic Au nanoparticles and found a 0.201 µmol g_{cat}^{-1} h^{-1} CO formation, at a high selectivity of *ca*. 87%.[149] Similar to Ag modified LDH (see 4.4), both materials band gaps, LDH (5.6 eV) and the Au SPR (3.1 – 3.2 eV), are excited. For the best performing sample towards CO formation, the Au deposition resulted in a reduction of the band gap to around 3 eV. Moreover, the charge transfer in the case of Au is different than in the case of Ag, since there is a difference in work function and SPR energy for Au (3.1 – 3.2 eV) and Ag (1.5 – 1.7 eV). This means that electrons in the $[Zn_3Ga(OH)_8]_2CO_3$ conduction band can be transferred to Au but not to Ag. It was shown that SPR electrons in Au excited by visible light cannot reduce CO_2, while the UV light band gap excited electrons in $[Zn_3Ga(OH)_8]_2CO_3$, which were subsequently transferred to Au, can be transferred to CO_2-derived species. The potential of excited electrons in Au is more positive than that of the excited electrons in the $[Zn_3Ga(OH)_8]_2CO_3$ conduction band, meaning that it is energetically more favourable to form CO rather than CH_3OH in the presence of UV light.

Blommaerts *et al*. used a Ti-Beta zeolite modified with Pt or Pd to shift the product selectivity from CO to CH_4. With a bare Ti-Beta

zeolite, a product selectivity of 70% CO and 30% CH_4 was obtained with a TOF towards CO around 43 µmol g_{cat}^{-1} h^{-1} under UVC irradiation, with a total power of 9.85 mW cm^{-2} at sample distance.[111] By adding Pt nanoparticles, the selectivity for CO was enhanced to 92% and the TOF highly increased to a value of 96 µmol g_{cat}^{-1} h^{-1}. Compared to P25 (10 µmol g_{cat}^{-1} h^{-1} CO) this is almost a ten-fold increase in TOF towards CO. The deposition of Pd instead of Pt completely inverts the selectivity towards 60% CH_4 and 40% CO.

Butburee *et al*. designed a novel type of complex heterostructures consisting of AuCu alloyed nanoprisms deposited between ZIF-8 nanoparticles and porous TiO_2 nanoplates.[150] The role of ZIF-8 was mainly to enhance the CO_2 capture, in order to increase the concentration on the surface of the catalyst (exemplified in Figure **11**), whereas the AuCu nanoprisms act as plasmonic centres to improve charge density and charge transfer to the CO_2 adsorption sites (Figure **11**, Model 3). This complex structure leads to a 7-fold increase in photocatalytic CO_2 reduction, in comparison with a reference catalyst containing no AuCu nanoprisms. In this way, a 92% selectivity towards CO was obtained with a TOF of 80 µmol g_{cat}^{-1} h^{-1}.
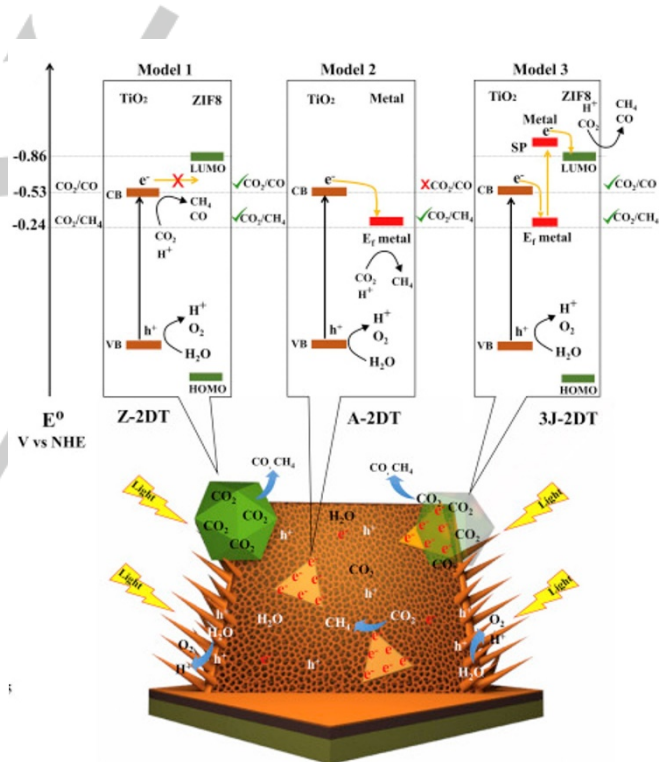
Figure 11. Graphical representation of the suggested mechanisms for CO_2 photoreduction in the presence of 2 components (Model 1, Model 2) and the highly efficient 3 components (Model 3). Reprinted with permission from ref.[150]

The following paragraphs will focus on both simple and more sophisticated systems involving plasmonic nanoparticles coupled with TiO_2. Cheng *et al*. used a dielectric barrier discharge cold plasma to reduce Ag nanoparticles on the surface of TiO_2 nanorods to achieve a high selectivity towards CO (~ 91%) under visible light illumination, using a 300 W Xe lamp with a 420 nm cut-off filter.[151] The small Ag nanoparticles, ~ 5.8 nm, increased the photocatalytic activity by playing a dual role, to achieve a TOF of 14.4 µmol g_{cat}^{-1} h^{-1}. First of all, they acted as electron sinks to

enhance separation of electron-hole pairs and thus preventing recombination. Secondly, the SPR effect induced activity under visible light and as a consequence enhanced the activity.

Zhao H. *et al*. used an interesting approach in which Au nanoparticles were decorated on a TiO_2 P25 photocatalyst.[152] By applying a very thin Al_2O_3 interlayer between Au and TiO_2, via atomic layer deposition (ALD), they achieved a high selectivity towards CO with a TOF of 9.75 µmol g_{cat}^{-1} h^{-1}. They aimed to unravel the plasmonic mechanism for the observed enhanced activity by changing the thickness of the interlayer and the size of the Au nanoparticles. Three main mechanisms were proposed to be responsible for the enhanced activity, SPR induced hot electron injection, near-field enhancement and enhanced charge separation. By applying an Al_2O_3 interlayer, direct electron transfer was inhibited and the electric field enhancement dampened. On the other hand, it was also found that the Al_2O_3 layer served as a passivation layer, thus reducing charge recombination. They designed several experiments to accurately elucidate on the contribution of each mechanism. First of all, they changed the size of the Au nanoparticles between 10, 20, and 30 nm. It was found that the highest activity resulted from the 10 nm Au samples. In theory, smaller nanoparticles have a slightly larger work function, and thus a larger Schottky barrier between Au and TiO_2.[153] This would mean that for smaller nanoparticles, the probability for the hot electron injection mechanism should be lower than for 30 nm nanoparticles. Since the activity is in the order Au_{10} > Au_{20} > Au_{30}, it was concluded that the hot electron injection mechanism did not contribute highly to the overall activity enhancement. The reason why samples with smaller Au particles were more active than the ones with larger nanoparticles was mainly attributed to a larger contact area and a more uniform distribution of the smaller particles (at a fixed weight ratio of $Au:TiO_2$). The very thin Al_2O_3 layer (0 – 5 nm) on the TiO_2 surface resulted in a substantial increase in CO production due to a reduced rate of electron-hole pair recombination, since it served as a passivation layer.[154–156] By deposition of a 0.5 nm Al_2O_3 interlayer, also more methane formation was observed in all samples. Since the reduction of CO_2 to CH_4 is an 8-electron reduction (6 electrons more in comparison with CO), more electrons are favourable to shift the selectivity to CH_4, which could be achieved by the passivation layer. However, once the Al_2O_3 layer became too thick (> 0.5 nm), the activity dropped again due to the blocking of electron transfer either to the adsorbed CO_2 molecules or Au, and dampening of the near-field effect in the case of Au. Lastly, FDTD simulations were performed to unravel the contribution of the near-field enhancement effect.[157] From the results in Figure **12**, it is clear that the larger the particles (in the studied 10-30 nm size range), the stronger the near-field enhancement, and the thicker the Al_2O_3 coating, the weaker the enhancement. Overall, since the enhancement is in the order of 10 000, the near-field enhancement is expected to contribute greatly to the photocatalytic activity, as was also shown by a thicker overcoat of Al_2O_3 that blocked the near-field enhancement with a loss of activity as a consequence. Moreover, the enhanced electric field can improve the charge separation effect from Au to TiO_2 by making it a field guided transfer, after which the gold nanoparticles can trap the electrons to extend their lifetime. In addition, this can also lead to an improved tunnelling through a thin Al_2O_3 layer (≤ 0.5 nm).
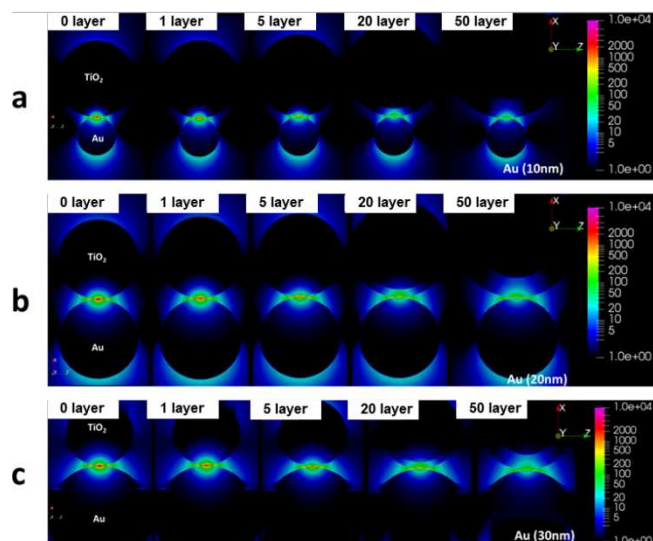
Figure 12. Near-field enhancement $|E|^2/|E_0|^2$ under 550 nm illumination as a result of FDTD simulations for (a) Au 10 nm, (b) Au 20 nm, and (c) Au 30 nm deposited on 20 nm TiO_2 particles with different thicknesses of Al_2O_3 overcoat. Reprinted with permission from ref.[152]

Wang *et al*. reached a comparable conclusion as Zhao *et al*. when taking into account different sizes of the Au plasmons deposited on TiO_2.[152,158] For the best performing sample, the authors report a production rate of 8.77 µmol g_{cat}^{-1} h^{-1} CO and 3.92 µmol g_{cat}^{-1} h^{-1} CH_4, under UV light (365 nm). The assumed reasons for the improved conversion in the presence of the sample with smaller and fewer Au plasmonic NPs are related to the more efficient *H production from H_2O, Ar-treatment by enhancing the electronic metal support interaction, as well as the lower loading, which may decrease the recombination rate.

In a recent study, Wang *et al*. compared the CO_2 photoconversion efficiency of Au plasmons deposited on 3 different types of TiO_2, varying the exposed facets, namely (101), (001) and co-existing (101) and (001).[159] Their findings suggest a clear superiority of Au-TiO_2 (101) facet exposed, due to the fact that the height of the Schottky barrier formed between Au-TiO_2 (101) is smaller than the one formed between Au-TiO_2 (001). For this reason, a more efficient transfer between CB e^- of TiO_2 to the Au co-catalyst is possible, under UV irradiation. At the same time, the hot electrons from plasmonic Au are more prone to migrate to the TiO_2, upon visible light irradiation. A maximum of 25.9 µmol g_{cat}^{-1} h^{-1} conversion rate towards CO and 5.3 µmol g_{cat}^{-1} h^{-1} towards CH_4 was achieved in the presence of Au-TiO_2 (101), upon UV light (320 < λ < 420 nm) illumination.

Cheng *et al*. showed that similar to the SiO_2 supports of Bera *et al*. and Mankidy *et al*., a specific amount of Al_2O_3 coated on the plasmon nanoparticles results in a positive effect on the overall CO_2 photoreduction activity.[137,138,151] The FDTD simulations performed by Li *et al*. and experimental photoreduction tests of Bera *et al*. showed similar behaviour when varying the particle size.[137,138,143]

Moreover, Li *et al*. proved the beneficial outcome of the addition of a thickness-controlled Al_2O_3 layer between Au/Cu nanoparticles and p-GaN.[160] The band structure and mechanism illustration comparison between Au/p-GaN and Cu/Au/Al_2O_3/p-GaN heterostructures (Figure **13** a) and b)) indicates that the Al_2O_3 may act as a recombination inhibitor, while the Cu addition increases the charge transfer efficiency, boosting the overall

reaction rate. The authors report a maximum CO production rate of approx. 600 µmol g_{cat}^{-1} h^{-1} in the presence of Cu/Au/Al$_2$O$_3$/p-GaN nanocomposite upon full-spectrum solar irradiation.
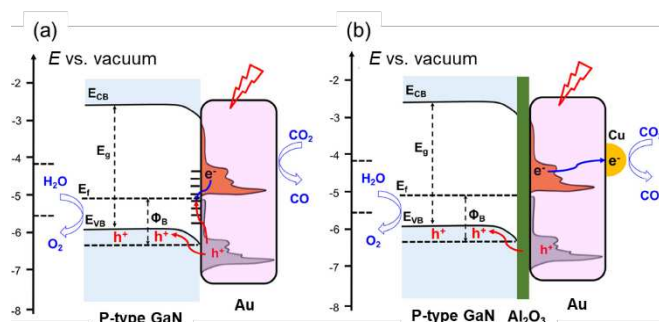
Figure 13. Schematic representation of band structure and photocatalytic mechanism of CO$_2$ conversion in the presence of H$_2$O for a) Au/p-GaN composite and b) Cu/Au/Al$_2$O$_3$/p-GaN nanoarchitecture. Reprinted with permission from ref.[160]

Shi *et al*. designed an attractive composite consisting of rutile TiO$_2$ (R-TiO$_2$) nanorod arrays modified with BiVO$_4$ quantum dots (QD).[161] On top, plasmonic Au nanoparticles were deposited. Under visible light (300 W Xe, λ > 420 nm), a TOF towards CO of 1 µmol cm^{-2} h^{-1} and a selectivity of ~ 80% was achieved. This activity was attributed to high visible light absorption and excellent charge carrier properties in the complex composite material. The conduction band of bulk BiVO$_4$ is located at 0 V, very close to the requirement for CO$_2$ reduction.[162–164] In the work of Shi *et al*. BiVO$_4$ QDs were used, having a band gap of 2.62 eV which is around 0.2 eV larger than bulk BiVO$_4$.[161] This means that the excited electrons in BiVO$_4$ QD are more energetic than in bulk BiVO$_4$ and energy transfer is therefore facilitated. As can be seen in Figure **14**, electrons excited in BiVO$_4$ QD are transferred to R-TiO$_2$ nanorods without significant energy loss since the difference in band gap of the two is insignificant, and subsequently transferred to Au, leading to an enhanced separation of charges and thus reduction of recombination. Furthermore, hot electrons excited on the Au nanoparticles due to the SPR effect can transfer to the R-TiO$_2$ nanorods.

As a final example, Samah *et al.* assembled a 3D flower-like nanocomposite, consisting of ZnO, CeO$_2$ and Ag plasmons for UV-vis assisted CO$_2$ photoreduction.[165] Here, the high conversion rate is attributed mostly to the formation of a Z-scheme mechanism, SPR effect and extended adsorption in the visible light region caused by the Ag nanoparticles as well as to the enhanced CO$_2$-nanocomposite interaction associated with the presence of CeO$_2$ and Ag plasmons. Once again, the good reactants adsorption was depicted as a very important factor, as suggested also by Jiang *et al.*.[135] The conversion rates towards CO and CH$_4$ reached a maximum of 75.5 µmol g_{cat}^{-1} h^{-1} and 4 µmol g_{cat}^{-1} h^{-1} respectively, in the presence 3% Ag-CeO$_2$-ZnO under simulated sunlight irradiation.

4.4. Methanol (CH$_3$OH) or ethanol (CH$_3$CH$_2$OH) as main products

Regarded as highly valued chemicals in industrial applications, CH$_3$OH and CH$_3$CH$_2$OH are very attractive products which may result from photocatalytic CO$_2$ reduction. Compared to CO and CH$_4$ gases, the aggregation state of these alcohols is liquid, thus offering a great advantage when the product separation process is discussed. Moreover, the transport and storage of liquid fuels is considerable less demanding and subject to a lower risk compared to the gaseous fuels.[166]

Li *et al.* used a complex system in which AgBr nanoparticles were deposited on g-C$_3$N$_4$-decorated nitrogen-doped graphene.[167] A Xe lamp with a 420 nm cut-off filter, at a total intensity of 150 mW cm^{-2}, was used to perform the CO$_2$ degradation experiments under visible light. This composite photocatalyst proved to be favourable for the reduction of CO$_2$ into hydrocarbon fuels, such as CH$_3$OH and CH$_3$CH$_2$OH, mostly due to its suitable energy band positions. The highest TOF towards CH$_3$CH$_2$OH was reported as 51 µmol g_{cat}^{-1} h^{-1}, while for CH$_3$OH a slightly lower TOF was achieved, 21 µmol g_{cat}^{-1} h^{-1}. The conduction band energy levels of AgBr (-0.8 eV vs. NHE) and graphitic-C$_3$N$_4$ (1.8 eV vs. NHE) as well as the valence band energy levels (-1.3 eV vs. NHE for AgBr and 1.4 eV vs. NHE for graphitic-C$_3$N$_4$) show a favourable position to allow visible light excitation.[168–170]
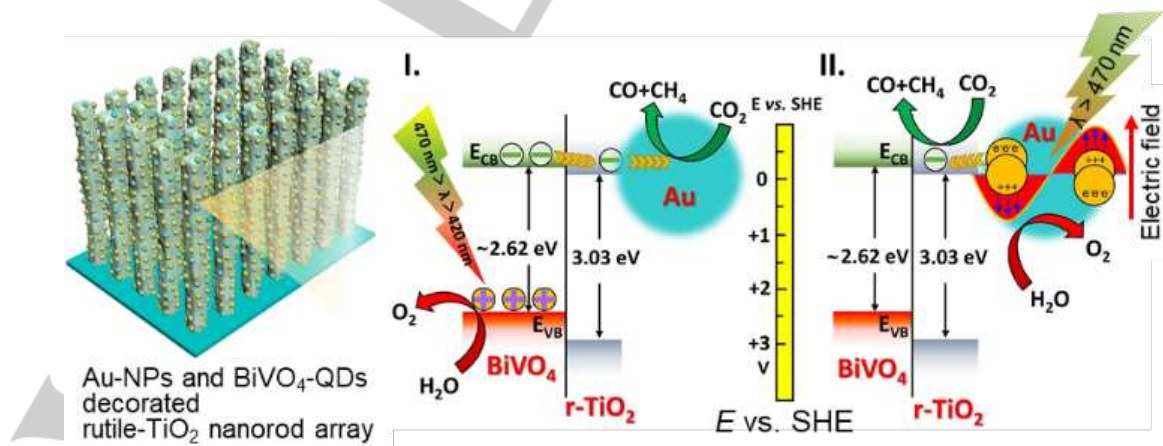
Figure 14. Schematic illustration of the mechanism for enhanced photocatalytic CO$_2$ reduction using Au/BiVO$_4$-QD/R-TiO$_2$. Reprinted with permission from ref.[161]

Since there are different possible sites on which AgBr nanoparticles are positioned in the g-C_3N_4-decorated nitrogen doped graphene, two distinct charge transfer mechanisms were proposed. In the first one, the AgBr nanoparticles are in contact with the graphitic-C_3N_4 upon the formation of a nanohybrid heterojunction. In the second mechanism, the AgBr nanoparticles are only located on the nitrogen-doped graphene. Upon irradiation with sufficient energy, the AgBr and graphitic-C_3N_4 are excited with the formation of electrons in the conduction band and holes in the valence band. The electrons in the conduction band of graphitic-C_3N_4 will then be transferred into the conduction band of AgBr and the holes in the valence band of AgBr will be injected in the valence band of g-C_3N_4. For the case of only AgBr nanoparticles on the nitrogen-doped graphene surface, the photocatalytic reactions will only occur on the AgBr surface. It is concluded, however, that this was not the main photocatalytic pathway in this semiconductor system since photoexcited electrons and holes migrate randomly leading to a high charge recombination probability, while the AgBr/g-C_3N_4-decorated nitrogen-doped graphene 'superhybrid' showed a preferable energy-gap-optimized combination.[171] Another possibility, where Ag^+ ions at the surface of AgBr are combined with accumulated electrons upon the formation of Ag^0 under visible-light illumination.[172] This would lead to the formation of a Z-scheme system, AgBr/Ag/graphitic-C_3N_4 similar to the one designed by Samah et al.[165] However, these two Z-scheme systems show a different role for Ag nanoparticles in the nanoarchitecture than the one reported by Murugesan et al. for AgCl/g-C_3N_4.[103] In the current study, an ohmic contact with low resistance can be formed with a high charge transfer rate, where electrons in the AgBr conduction band can recombine with holes from the g-C_3N_4 valence band on the Ag^0 sites.[96,173] As a consequence, holes in the AgBr valence band and electrons in the graphitic-C_3N_4 conduction band are solely available for degradation and reduction reactions. Finally, in the last mechanism, the SPR effect of metallic silver is exploited to enhance the photocatalytic activity. An et al. performed a CO_2 reduction experiment using plasmonic AgX:Ag (X = Cl, Br) nanoparticles, synthesized by a glycerol-mediated solution route.[174] They performed the experiment under visible light (300 W Xe arc lamp with a UV cut-off filter at 400 nm) in a 0.1 M $NaHCO_3$ solution, bubbled with pure CO_2 (99.995%) for 10 min at a flow rate of 0.7 L min^{-1}, achieving high selectivity towards CH_4, reaching 37 $\mu mol\ g_{cat}^{-1}\ h^{-1}$ for the AgCl:Ag system. In a similar manner, Cai et al. used a Ag/AgCl plasmonic photocatalyst for the synthesis of liquid fuels from CO_2.[175] The reaction was performed using a 500 W Xe lamp equipped with a 420 nm cut-off filter. Both CH_3CH_2OH and CH_3OH were produced with a slightly higher selectivity towards CH_3CH_2OH. The highest turnover frequency towards CH_3CH_2OH was 45 $\mu mol\ g_{cat}^{-1}\ h^{-1}$ vs. 30 $\mu mol\ g_{cat}^{-1}\ h^{-1}$ for CH_3OH. In addition to the improved light harvesting and strong ability of Ag plasmons to reduce CO_2 as reported by An et al., Cai et al. highlighted the suitable positions of the band energies to create a strong electronic coupling between Ag plasmons and the AgCl semiconductor, thus considerably improving the transfer of the photogenerated electrons from Ag to AgCl.[174,175] Moreover, the later study showed that a Mie scattering effect caused by the diversity of the particle morphologies plays a very important role in the CO_2 photoreducing ability of a catalyst.

Kawamura et al. modified $[Zn_3Ga(OH)_8]_2CO_3.mH_2O$ LDH with plasmonic Ag nanoparticles.[149] Relatively low TOFs were obtained towards CH_3OH and CO. Using $Ag/[Zn_3Ga(OH)_8]_2CO_3.mH_2O$, they obtained a value of 0.118 $\mu mol\ g_{cat}^{-1}\ h^{-1}$ for CH_3OH with a selectivity of 54%. Based on these results, the authors assume that by irradiating with UV and visible light, both the band gap of $[Zn_3Ga(OH)_8]_2CO_3$ (5.6 eV) and the SPR Ag (1.5 – 1.7 eV) are excited. It is worth mentioning that for the best performing catalyst towards CH_3OH $(Ag/[Zn_3Ga(OH)_8]_2CO_3.mH_2O)$ no similar reduction of the band gap was observed as in the case of Au. This may be related to the fact that the samples were prepared via different pathways, thus forming unique self-assemblies. The authors suggest that the charge transfer occurs from the Ag SPR-excited electrons to the conduction band of $[Zn_3Ga(OH)_8]_2CO_3$ LDH.

Liu et al. synthesized plasmonic Ag modified TiO_2 nano-wire films to enhance the production of CH_3OH.[176] Under UV (16 W Hg lamp) and Vis (500 W Xe lamp, 420 nm cut-off filter) irradiation, they achieved a CH_3OH production rate of 2.8 $\mu mol\ cm_{cat}^{-2}\ h^{-1}$. At the same time, they showed that a synergistic effect between the SPR of Ag and the charge transfer property from TiO_2 to Ag exist in the Ag/TiO_2 system. Firstly, photoexcited electrons in TiO_2 (due to UV irradiation) were transferred to the Ag nanoparticles. Then, due to the strong electric field from the SPR effect, the energy of the trapped electrons is enhanced, resulting in a facile reaction between the electrons and adsorbed CO_2 molecules. The holes in the valence band of TiO_2 can oxidize water to form $\cdot OH$ radicals, which in turn can release H^+ and O_2.[177] These H^+ ions and electrons are then used to produce CH_3OH. Same Liu et al.[178] used TiO_2 nanoflowers as support for plasmonic Cu nanoparticles to enhance the production of CH_3OH. They achieved a CH_3OH production rate of 1.8 $\mu mol\ cm_{cat}^{-2}\ h^{-1}$ for Cu/TiO_2, which was a 6-fold increase in comparison with the bare TiO_2 film. The suggested mechanism is similar to the previous study, where Ag/TiO_2 nano-wire films were used.[176]

Wang et al. used visible light at elevated temperature (220 °C) to study the CH_3OH formation in the presence of Cu nanoparticles deposited on ZnO, CeO_2, TiO_2 and ZrO_2.[179] Remarkable results were obtained for the Cu/ZnO system, while low to negligible yields were observed for Cu/CeO_2, Cu/TiO_2 and Cu/ZrO_2, respectively. The activation of the Cu/ZnO catalyst for the selective reduction of CO_2 towards CH_3OH led to a TOF of 48 $\mu mol\ g_{cat}^{-1}\ h^{-1}$. The authors performed both theoretical and experimental studies to elaborate on the possible mechanism. Furthermore, they performed the experiments at elevated temperature (220 °C) to distinguish between a purely thermal route and a photo-thermal route. At the same time, the authors proved that CH_3OH is formed via a series of intermediates ($\cdot HCOO$, $\cdot HCOOH$, $\cdot H_2COOH$, and $\cdot CH_3O$) in the purely thermal route, of which the rate limiting step was the hydrogenation of $\cdot HCOOH$. In-situ diffuse reflectance infrared Fourier transform spectroscopy (DRIFT) showed that only $\cdot HCOO$ and $\cdot CH_3O$ species were present, since they adsorb more strongly.[180,181] A similar route is observed in the case of the photo-thermal process, however, the electrons and holes pathways are different.

Yadav et al. reached high selectivity towards CH_3OH, with no formation of CO or CH_4, using a 1 wt% plasmonic Au/$Ti_{0.72}Si_{0.28}O_2$ under visible light irradiation (six 7 W LEDs, 80 W m^{-2}).[182] They optimized the amount of Si in the TiO_2 lattice in order to obtain the highest possible CO_2 adsorption. The TOF towards CH_3OH was 38 $\mu mol\ g_{cat}^{-1}\ h^{-1}$. They explain the higher activity of the Au/$Ti_{0.72}Si_{0.28}O_2$ sample in comparison with other Au/$Ti_xSi_{1-x}O_2$ samples as follows: the isoelectric point of oxides is known within

a relatively small range, e.g. 2-3 for SiO_2 and 5-7 for TiO_2, a combination of SiO_2 and TiO_2 in the support would lead to a lower isoelectric point as the amount of SiO_2 increases.[183] Au nanoparticles with a size of 4.9 have a isoelectric point of 5.5.[184] Taking this into account, the TiO_2 with the highest SiO_2 doping in this study ($Au/Ti_{0.72}Si_{0.28}O_2$) has the best interaction with Au nanoparticles, leading to the most stable and best dispersed Au nanoparticles. Furthermore, the better adsorption of CO_2 can also explain the higher activity. This was confirmed by DFT calculations, where a TiO_2 (101) surface interaction with CO_2 had an adsorption energy of -0.12 eV, while in the case of Si doped TiO_2 (101) the adsorption energy was -0.28 eV, showing a stronger adsorption. In addition, the CO_2 uptake experiments proved that an increasing amount of Si in $Au/Ti_xSi_{1-x}O_2$ resulted in an increase of CO_2 uptake. Lastly, it was shown that also a plasmonic effect in the form of hot electron injection boosted the photocatalytic activity.

In a recent study, Becerra et al. obtained remarkable amounts of CH_3OH and CH_3CH_2OH, while demonstrating the importance of a high quality support for the incorporation of plasmonic Au nanoparticles for CO_2 reduction applications.[185] More specifically, their system consisted of a zeolitic imidazole framework (ZIF-67) as support with a very high surface area (~ 1600 m^2/g), coupled with x% wt Au nanoparticles (x = 5, 10, 20, 30). The conversion rates reached ~ 2.5 mmol g^{-1} h^{-1} for CH_3OH in the presence of Au_{10}@ZIF-67 and ~ 0.5 mmol g^{-1} h^{-1} CH_3CH_2OH for Au_{20}@ZIF-67, under simulated solar light irradiation. Similar to Yadav et al.[182] and Butburee et al., Becerra et al. assign part of the enhanced activity to the good interaction of CO_2 with the support material, in particular to the derived Lewis acid/basic sites influenced by the presence of Co^{2+} clusters and to the presence of imidazole C=N bond, which is beneficial for CO_2 and H_2O surface adsorption.[150,185]

Non noble metallic building blocks like $SrTiO_3$ (La Cr) (STO), Cu, Ni and TiN were used by Yu et al. to reach an increased amount of CH_3CH_2OH under full solar irradiation.[186] The reported CH_3CH_2OH production rate for the best photocatalyst reached 21.3 µmol g_{cat}^{-1} h^{-1} with a selectivity of 79%. Following a series of experiments, the authors proved that the presence of Cu nanoparticles has multiple roles, being involved in the hot electrons generation due to their LSPR, as well as behaving as an electron highway for the photogenerated carriers. At the same time, the TiN nanoparticles are also implicated in two different mechanisms, such as the hot electrons generation via LSPR and the improvement of the overall catalyst-light interaction, caused by the remarkable TiN NPs light absorbance capacity. Moreover, the STO support is capable of providing photogenerated carriers able to photoreduce CO_2 to CH_3CH_2OH, while Ni is positively affecting the light absorption capacity of the catalyst. Finally, the interface created between Cu and Ni (Cu@Ni) proved to be highly important for the conversion of CO_2 to CH_3CH_2OH. Figure 15 highlights the CO_2 to CH_3CH_2OH reaction pathways with regard to the calculated free energy barrier (eV), at the Co@Ni interface. Firstly, the authors suggest that the main advantage of the Cu@Ni interface is the decrease of the activation energy of CO_2 from 1.31 eV for Cu surface to 1.28 eV for Cu@Ni interface. Secondly, the production of C2 compounds is enhanced by the fact that CO* desorbs considerably less well from the Cu@Ni interface (G_{abs} = -1.39 eV) than from the Cu surface (G_{abs} = -0.58 eV).
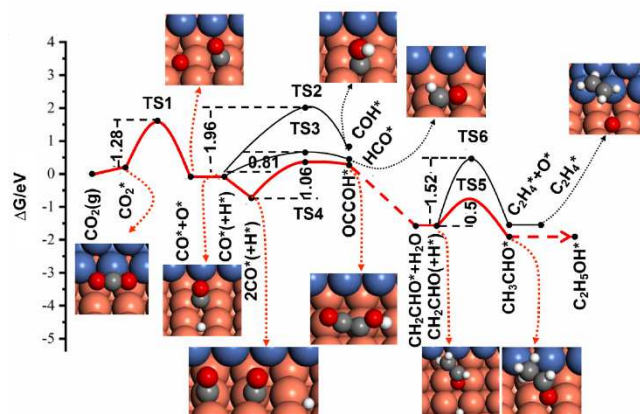
Figure 15. Schematic representation of the free energy diagram to reduce CO_2 to CH_3CH_2OH and ethene at the interface of Cu@Ni. Reprinted with permission from ref.[186]

Table **1** summarizes a series of literature studies on plasmon-enhanced photocatalyst systems for CO_2 reduction towards CH_4, CO, CH_3OH/CH_3CH_2OH.

Table 1. Plasmon-enhanced photocatalytic systems for CO_2 reduction.

Material	Experimental details	Products	Yield/TOF (µmol g_{cat}^{-1} h^{-1})	Ref.
AgX:Ag (X = Cl, Br)	CO_2 dissolved in H_2O (+ 0.1 M $NaHCO_3$); 300 W Xe, 400 nm cut-off filter	CH_3OH	37	[174]
Ag/AgBr-CNT	0.2 M $KHCO_3$ in H_2O; 150 W Xe 420 nm cut-off 25 mW cm^{-2}	CH_4	30	[92]
Ag/AgCl	CO_2 dissolved in H_2O (0.1 M $NaHCO_3$); 500 W Xe lamp, 420 nm cut-off filter	C_2H_5OH	45	[175]
		CH_3OH	30	
Ag/AgIO₃	CO_2 saturated water vapor; 500 W Xe lamp, 400 nm cut-off filter	CH_4	6	[107]
AgBr Supported on Graphitic-C3N4-Decorated N-Doped Graphene	CO_2 dissolved in H_2O (+ 0.1 M $NaHCO_3$); Xe lamp, 420 nm cut-off filter (150 mW cm^{-2})	C_2H_5OH	51	[167]
		CH_3OH	21	
Ag/ZnIn₂S₄/TiO_2	CO_2 saturated water vapor; 300 W Xe lamp (280 nm < lambda < 780 nm)	CH_4	6290 ppm g^{-1} h^{-1}	[134]
Ag/TiO_2-nano-wire	CO_2 saturated water vapor; 16W Hg (UV) + 500 W	CH_3OH	2.8	[176]

Catalyst	Conditions	Product	Value	Ref.
Ag/TiO$_2$	Xe 420 nm cut-off (VIS) CO$_2$ saturated water vapor; 300 W Xe 420 nm cut-off	CH$_4$	1.6	[112]
Ag/[Zn$_3$Ga(OH)$_8$]$_2$CO$_3$.mH$_2$O	H$_2$; 500 W Xe (42 mW cm^{-2})	CH$_3$OH	0.118	[149]
AgBr/g-C3N4	CO$_2$ saturated water vapor; 15 W daylight (8.5 mW cm^{-2})	CH$_4$	1.3	[102]
Ag/TiO$_2$	H$_2$O gas phase; 300 W Xe	CH$_4$	1.4	[113]
	CO$_2$ dissolved in H$_2$O (+ 1 M NaHCO$_3$); 300 W Xe	CH$_3$OH	4.2	
Ag/Ag$_2$SO$_3$	CO$_2$ saturated water vapor; 500 W Xe 400 nm cut-off (10.75 mW cm^{-2})	CH$_4$ (70%)	3	[108]
		CO (30%)	1.24	
Ag/TiO$_2$ NR	CO$_2$ saturated water vapor; 300 W Xe 420 cut-off	CO	14.4	[151]
Ag/TiO$_2$	H$_2$O vapor; 200 W Xe/Hg	CH$_4$	8.75 ppm h^{-1}	[114]
Ag/TiO$_2$ NT arrays	H$_2$O vapor; 300 W Xe, 400 nm cut-off	CH$_4$	50 mmol h^{-1} m^{-2}	[115]
AgCl/g-C3N4	Aqueous medium (H$_2$O); 11W fluorescent lamp	CH$_4$	6.6	[103]
Ag/TiO$_2$ (anatase)	7.25 (CO$_2$:H$_2$O); 24W 365 nm lamp, 47.23 W m^{-2}	CH$_4$	5.8	[116]
	30W LED, cut-off 400 or 455, 53.98 W m^{-2}	CH$_3$OH	0.2	
Ag/3D porous ZnO nanosheets	H$_2$O; 300W Xe; 545 mW/cm^2	CO	25	[110]
Ag/TiO$_2$ core-shell	H$_2$O vapor; AM1.5 300 W	CH$_4$	5	[127]
Ag/SrTiO$_3$ nanocubes	H$_2$O; 300W Xe 420 nm cut-off	CO	80 µmol g^{-1}	[145]
Au/TiO$_2$/W$_{18}$O$_{49}$	H$_2$O; 50 mW/cm^2; vis-NIR, cut-off 420 nm	CH$_4$	35.55	[135]
Au/TiO$_2$	CO$_2$ saturated water vapor; 532 nm laser, 350 mW cm^{-2}	CH$_4$	1.5 µmol m^{-2} h^{-1}	[128]
	254 nm, 20 mW cm^{-2}	CH$_4$, C$_2$H$_6$, HCHO, CH$_3$OH	15 µmol m^{-2} h^{-1} (CH$_4$)	
	365 nm, 20 mW cm^{-2}	CH$_4$	1.3 µmol m^{-2} h^{-1}	
Au/ZrO$_2$	H$_2$O; 300 W Xe-lamp (AM 1.5G filter, solar simulator), 100 mW/cm^2	CO	25.6	[146]
		CH$_4$	5.1	
Au/ZnO	H$_2$; cw 532 nm laser 80 x 10^4 W m^{-2}	CO	4	[67]
		CH$_4$	1.3	
Au/[Zn$_3$Ga(OH)$_8$]2CO$_3$.mH$_2$O	H$_2$; 500 W Xe (42 mW cm^{-2})	CO	0.201	[149]
Au/TiO$_2$	H$_2$O vapor; 200 W Xe/Hg	CH$_4$	2.8 ppm h^{-1}	[114]
Au/g-C3N4	CO$_2$ saturated water vapor; 300 W Xe	CO	6.6	[142]
		CH$_4$	1.55	
Au/TiO$_2$/BiVO$_4$	CO$_2$ saturated water vapor; 300 W Xe	CH$_4$	16.25	[136]
Au/P-doped g-C3N4	H$_2$O; 300W Xe, 420 nm cut-off	CH$_4$	24	[106]
Au/Al$_2$O$_3$/TiO$_2$	CO$_2$ saturated water vapor; 450W Xe	CO	9.75	[152]
0.74 wt% Au/TiO$_{2-x}$	H$_2$O; UV (365 nm LED); ~ 49.5 mW cm^{-2}	CO	8.77	[158]
		CH$_4$	3.92	
Au-TiO$_2$ (101)	H$_2$O; UV cutoff filter 320 < λ < 420 nm; 33 mW cm^{-2}	CO	25.9	[159]
		CH$_4$	5.3	
Cu/Au/Al$_2$O$_3$/p-GaN	H$_2$O; solar simulator 75W, 1.5 AM	CO	~600	[160]
Au/Ti$_{0.72}$Si$_{0.28}$O$_2$	H$_2$O; 6 7W LED (visible); 80 W m^{-2}	CH$_3$OH	38	[182]
Au$_{10}$@ZIF-67	H$_2$O; solar simulator; 150 mW cm^{-2}	CH$_3$OH	2500	[185]
Au$_{20}$@ZIF-67	H$_2$O; solar simulator; 150 mW cm^{-2}	CH$_3$CH$_2$OH	500	[185]
Au/BiVO$_4$ quantum dot/rutile-TiO$_2$ nanorod array	H$_2$O; 300W Xe, 420 nm cut-off	CO	1 µmol cm^{-2} h^{-1}	[161]
3% Ag-CeO$_2$-ZnO	H$_2$O gas; simulated sunlight; 300W xenon lamp	CO	75.5	[165]

19

Catalyst	Conditions	Product	Value	Ref.
		CH_4	4	
Au/g-C3N4	CO_2 saturated water vapor; 8 W Hg	CO	10	[143]
		CH_4	4.75	
Au/3D porous ZnO nanosheets	H_2O; 300W Xe; 545 mW/cm^2	C_2H_6	27	[110]
0D/2D Au/TiO2	H_2O vapor; 300W Xe	CH_4	70.34	[129]
Au/TiO2 NTA	CO_2 saturated water vapor; 300W Xe	CH_4	/	[130]
Au-TiO2	H_2O; solar simulator AM 1.5 G, 100 mW^{-2}	CH_4	302	[131]
Au/g-C3N4	H_2O; Xe lamp	CO	28.3	[144]
Cu/TiO2	CO_2 dissolved in H_2O; 365 nm, 3.25 mW cm^{-2}	CH_4	2.91 ppm g^{-1} h^{-1}	[139]
Ag@SiO2/Ag-Pt/TiO2	H_2O; 100 W Hg lamp	CH_4	/	[138]
Columnar Cu/porous TiO2	CO_2 saturated water vapor; AM1.5 100 mW cm^{-2}	CH_4	124.3 ppm cm^{-2} h^{-1}	[140]
Cu/TiO2-nanoflower	CO_2 saturated water vapor; 16W Hg (UV) + 500 W Xe 420 nm cut-off (VIS)	CH_3OH	1.8 µmol cm^{-2} h^{-1}	[178]
Au@SiO2/Pt/TiO2	CO_2 saturated water vapor; 365 nm and 530 anm LED	CH_4	2.98	[137]
Pd/3D porous ZnO nanosheets	H_2O; 300W Xe; 545 mW/cm^2	CH_4	18	[110]
Cu/ZnO	H_2; Xe lamp, 0.58 W cm^{-2} 420 nm cut-off	CH_3OH	48	[179]
AuCu/TiO2/ZIF-8	H_2O; AM1.5 Xe lamp	CO	80	[150]
Au-Pd/TiO2	CO_2 saturated water vapor; 300W Xe	CH_4	47	[132]
Pt/Ti-Beta zeolite	30% CO_2; 10% H_2; 9.85 mW cm^{-2} UVC	CO	96	[111]
Pd/Ti-Beta zeolite	30% CO_2; 10% H_2; 9.85 mW cm^{-2} UVC	CH_4	51	[111]
Al/Cu2O	CO_2:H_2 1:1; visible light laser up to 10 w cm^{-2}	CO	0.1 µmol g^{-1} s^{-1}	[148]
SrTiO3 (La Cr)/Cu @ Ni/TiN	H_2O; 300 W Xe lamp; 600 mW/cm^2	CH_3CH_2OH	21.3	[186]

5. Summary and Conclusions

This review aims to provide a case-based concise overview of the efforts made by the research community in the field of plasmon-enhanced semiconductor photocatalytic CO_2 conversion, potentially a highly sustainable CO_2 reduction technology since it can operate entirely under solar light. After a brief introduction on plasmonic photocatalysis, in particular for the CO_2 reduction reaction, the first part of the review covers a series of studies reporting methane as main product of the CO_2 photoreduction. In the second part of the review, the focus lies on literature papers covering carbon monoxide as main product of the CO_2 photoreduction, while the third and final part targets a collection of studies describing liquid fuels, methanol and ethanol as main product of the CO_2 photoreduction.

In general, and perhaps surprisingly, no clear trends towards specific end products were observed when using different supports decorated with Ag or Au plasmonic nanostructures. A limited number of studies reported the shift of the selectivity towards CH_4 from CO, when Pt was deposited on the supports. Similar, the use of Pd showed the preference for CH_4 product formation. The main limitation of the CO_2 photoreduction remains the product formation rate that is only in the order of a few tens of µmol g$_{cat}^{-1}$ h^{-1} for most of the studies, while only recently the highest yield reached just below 2500 µmol g$_{cat}^{-1}$ h^{-1} CH_3OH.[185] The majority of research still focuses on the use of TiO2-based photocatalysts, however it seems that the limit in this case is almost reached and a series of papers report considerable higher conversion rates when other than TiO2 materials are used.[160],[185] A shift towards other semiconductor materials can potentially prelude a breakthrough as they may offer higher selectivities and lower recombination rates.

What is also clear from this review, is that yet a lot needs to be learned on the CO_2 reduction mechanism. Fully unravelling the different possible pathways in different reaction conditions can offer great insights and important building blocks to select the most optimal combination of materials for certain applications. In addition, in the field of plasmonic photocatalysis, there is still a lot of debate regarding the different operating mechanisms. It would represent a step forward to unravel the dominant mechanism under different process conditions and for different materials. On the other hand, it is of crucial importance that the researchers critically analyse and report their results in order to not promote inaccurate interpretations.

Up to now, it is shown that an improved overlap of the plasmon absorption band and the band gap energy of the semiconductor may enhance the photoactivity. This can be controlled by a careful selection of which plasmons to be used and their respective sizes or shapes. Relative smaller plasmon nanoparticles have a better separation efficiency of electron-hole pairs and thus lead to reduced recombination, while relative larger plasmonic particles may produce a stronger near-field enhancement. For this reason, the accurate control over the size and shape of plasmonic nanoparticles must remain a priority when designing new plasmon-based photocatalysts. In case of Bera et al., the gradual increase of Au NPs from 4 to 26 nm showed a maximum LSPR for 18 nm.[137] On the contrary, in the system of Li et al. the highest photoconversion was obtained in the presence of Au NPs with a narrow distribution between 2-8 nm (approx. 20% 2-4 nm, 56% 4-6 nm and 22% 6-8 nm) when compared with 2 to 6 nm (approx. 76% 2-4 nm and 24% 4-6 nm) and bigger Au NPs 6 to 12 nm or 6 to 14 nm (broader distributions for the latter ones).[143] Moreover, a series of studies included in this review explain the need of UV

light in order to obtain significant amounts of multi-electron reactions towards methanol and methane. At the same time, synergistic yields towards high value products were observed when UV and visible light were coupled, compared to the sum of the yields obtained under UV and visible light irradiation separately. It is also worth noting that during the photoreduction process, a strong interaction of CO* radicals with the active sites of the catalysts increases the selectivity for the formation of C2 products.[186] As a consequence, one can design a more efficient photocatalytic material able to reduce CO_2 towards ideally ethanol, by taking into account not only the multi-electron reaction required to form ethanol, but also the C-C coupling reaction which must take place and can be controlled by the interaction of the catalyst active sites with the CO* radicals. Furthermore, in the field of plasmonic photocatalytic CO_2 reduction one of the most important aspects to focus on in future research is the synthesis of highly stable non-noble metal nanoparticles such as Cu, Ni and Al. Although some publications already report on the use of Cu, Ni and Al, there is still a lot of work to be done to unravel a widely applicable and scalable synthesis route and to ensure the long-term stability of such nanoparticles. At the same time, the stability of non-noble metals is considerably lower to that of noble metals, due to the formation of oxide layers. In some cases these oxide layers may positively influence the properties of the photocatalyst or, in most of the cases, negatively affect the process. In order to avoid this, protective layers of carbon-based supports (even MOFs) or polymers may be applied on the surface of the nanoparticles. The organic-based supports can be specifically tuned to interact with the CO_2 molecules and offer the advantage of a very high surface area, which increases the number of active sites. In addition, controlled atomic layer deposition (ALD) or development of core-shell designs are able to tackle the surface stability disadvantage found for many non-noble metal nanoparticles. As a step by step process, an elegant practice to limit the use of noble metal plasmons is to create bimetallic alloys consisting of non-noble metals and reduced amounts of noble metals. In this way, also the relatively low stability of the non-noble metal may be improved and the catalyst may undergo many cycles of use. Another and maybe even more promising approach involves the use of two non-noble metals simultaneously, which proved to reduce the activation energy of CO_2 at the created interface, compared to the energy required to activate CO_2 at the surface of each non-noble metal. In this case, the use of noble metals is completely avoided and the costs of the catalyst may be reduced considerably, while the recyclability is strongly increased. To conclude, an important aspect that is not covered in this review, is (photo)reactor engineering. However, a high potential still remains in this field especially considering aspects such as optimized (solar) light utilization and maximizing the contact time between reagents and photocatalyst, with a low pressure drop in the best case. On the other hand, it is already virtually impossible to accurately compare the results obtained from different studies, due to the wide variety of reactor systems and reaction conditions used (and not always accurately reported). In that sense, it is equally important for the photocatalytic community to evolve towards a more standardized method of recording and reporting the yields. All in all, we notice rapid advancements in all these different aspects of light-driven CO_2 conversion, and are therefore definitely expecting important breakthroughs in the coming years.

1   S. N. Habisreutinger, L. Schmidt-Mende and J. K. Stolarczyk, *Angew. Chemie Int. Ed.*, **2013**, *52*, 7372–7408.

2   J. Ran, T. Y. Ma, G. Gao, X.-W. Du and S. Z. Qiao, *Energy Environ. Sci.*, **2015**, *8*, 3708–3717.

3   X. Chang, T. Wang and J. Gong, *Energy Environ. Sci.*, **2016**, *9*, 2177–2196.

4   M.-Q. Yang and Y.-J. Xu, *Nanoscale Horizons*, **2016**, *1*, 185–200.

5   N. S. Lewis and D. G. Nocera, *Proc. Natl. Acad. Sci.*, **2006**, *103*, 15729 **LP** – 15735.

6   P. D. Tran, L. H. Wong, J. Barber and J. S. C. Loo, *Energy Environ. Sci.*, **2012**, *5*, 5902–5918.

7   BP, *The BP Energy Outlook 2030*, **2013**.

8   M. Marszewski, S. Cao, J. Yu and M. Jaroniec, *Mater. Horizons*, **2015**, *2*, 261–278.

9   K. Li, X. An, K. H. Park, M. Khraisheh and J. Tang, *Catal. Today*, **2014**, *224*, 3–12.

10   G. Centi and S. Perathoner, *ChemSusChem*, **2010**, *3*, 195–208.

11   Y. Qu and X. Duan, *Chem. Soc. Rev.*, **2013**, *42*, 2568–2580.

12   T. Hisatomi, J. Kubota and K. Domen, *Chem. Soc. Rev.*, **2014**, *43*, 7520–7535.

13   X. Chen, S. Shen, L. Guo and S. S. Mao, *Chem. Rev.*, **2010**, *110*, 6503–6570.

14   K. Li, B. Peng and T. Peng, *ACS Catal.*, **2016**, *6*, 7485–7527.

15   H. Abdullah, M. M. R. Khan, H. R. Ong and Z. Yaakob, *J. CO2 Util.*, **2017**, *22*, 15–32.

16   J.-M. Herrmann, *Catal. Today*, **1999**, *53*, 115–129.

17   O. Carp, C. L. Huisman and A. Reller, *Prog. Solid State Chem.*, **2004**, *32*, 33–177.

18   A. Mills and S. Le Hunte, *J. Photochem. Photobiol. A Chem.*, **1997**, *108*, 1–35.

19   D. Mardare, M. Tasca, M. Delibas and G. I. Rusu, *Appl. Surf. Sci.*, **2000**, *156*, 200–206.

20   M. Pelaez, N. T. Nolan, S. C. Pillai, M. K. Seery, P. Falaras, A. G. Kontos, P. S. M. Dunlop, J. W. J. Hamilton, J. A. Byrne, K. O'Shea, M. H. Entezari and D. D. Dionysiou, *Appl. Catal. B Environ.*, **2012**, *125*, 331–349.

21   A. Gołąbiewska, M. P. Kobylański and A. Zaleska-Medynska, in *Metal Oxides*, ed. A. B. T.-M. O.-B. P. Zaleska-Medynska, Elsevier, 2018, pp. 3–50.

22   S. Linic, P. Christopher and D. B. Ingram, *Nat. Mater.*, **2011**, *10*, 911.

23   K. L. Kelly, E. Coronado, L. L. Zhao and G. C. Schatz, *J. Phys. Chem. B*, **2003**, *107*, 668–677.

24   G. Mie, *Ann. Phys.*, **1908**, *330*, 377–445.

25   S. K. Ghosh and T. Pal, *Chem. Rev.*, **2007**, *107*, 4797–4862.

26   S. Link and M. A. El-Sayed, *J. Phys. Chem. B*, **1999**, *103*, 4212–4217.

27   S. Link and M. A. El-Sayed, *Int. Rev. Phys. Chem.*, **2000**, *19*, 409–453.

28   X. Zhou, G. Liu, J. Yu and W. Fan, *J. Mater. Chem.*, **2012**, *22*, 21337–21354.

29   L. M. Liz-Marzán, *Langmuir*, **2006**, *22*, 32–41.

30   M. A. Garcia, *J. Phys. D. Appl. Phys.*, **2012**, *45*, 389501.

31   D. D. Evanoff and G. Chumanov, *J. Phys. Chem. B*, **2004**, *108*, 13957–13962.

32   H. A. Atwater and A. Polman, *Nat Mater*, **2010**, *9*, 205–213.

33   D. B. Ingram, P. Christopher, J. L. Bauer and S. Linic, *ACS Catal.*, **2011**, *1*, 1441–1447.

34   Z. Wang, J. Liu and W. Chen, *Dalt. Trans.*, **2012**, *41*, 4866–4870.

35   X. Zhang, Y. L. Chen, R.-S. Liu and D. P. Tsai, *Reports Prog. Phys.*, **2013**, *76*, 46401.

36   C. Clavero, *Nat. Photonics*, **2014**, *8*, 95.

37   M. L. Brongersma, N. J. Halas and P. Nordlander, *Nat. Nanotechnol.*, **2015**, *10*, 25.

38   T. P. White and K. R. Catchpole, *Appl. Phys. Lett.*, **2012**, *101*, 073905.

39   H. Lee, Y. K. Lee, E. Hwang and J. Y. Park, *J. Phys. Chem. C*, **2014**, *118*, 5650–5656.

40   N. Szydlo and R. Poirier, *J. Appl. Phys.*, **1980**, *51*, 3310–3312.

41   S. Mubeen, G. Hernandez-Sosa, D. Moses, J. Lee and M. Moskovits, *Nano Lett.*, **2011**, *11*, 5548–5552.

42   M. Moskovits, *Science (80-.).*, **2011**, *332*, 676 **LP** – 677.

43   N. Blommaerts, R. Asapu, N. Claes, S. Bals, S. Lenaerts and S. W. Verbruggen, *Chem. Eng. J.*, **2017**, *316*, 850–856.

44   J. Fang, S.-W. Cao, Z. Wang, M. M. Shahjamali, S. C. J. Loo, J. Barber and C. Xue, *Int. J. Hydrogen Energy*, **2012**, *37*, 17853–17861.

45   A. Tanaka, K. Hashimoto and H. Kominami, *Chem. Commun.*, **2017**, *53*, 4759–4762.

46   A. Tanaka, K. Fuku, T. Nishi, K. Hashimoto and H. Kominami, *J. Phys. Chem. C*, **2013**, *117*, 16983–16989.

47   H. Wang, T. You, W. Shi, J. Li and L. Guo, *J. Phys. Chem. C*, **2012**, *116*, 6490–6494.

48   P. Wang, B. Huang, Y. Dai and M.-H. Whangbo, *Phys. Chem. Chem. Phys.*, **2012**, *14*, 9813–9825.

49   R. Asapu, N. Claes, S. Bals, S. Denys, C. Detavernier, S. Lenaerts and S. W. Verbruggen, *Appl. Catal. B Environ.*, **2017**, *200*, 31–38.

50   S. W. Verbruggen, M. Keulemans, B. Goris, N. Blommaerts, S. Bals, J. A. Martens and S. Lenaerts, *Appl. Catal. B Environ.*, **2016**, *188*, 147–153.

51   S. W. Verbruggen, M. Keulemans, M. Filippousi, D. Flahaut, G. Van Tendeloo, S. Lacombe, J. A. Martens and S. Lenaerts, *Appl. Catal. B Environ.*, **2014**, *156–157*, 116–121.

52   H. Peeters, M. Keulemans, G. Nuyts, F. Vanmeert, C. Li, M. Minjauw, C. Detavernier, S. Bals, S. Lenaerts and S. W. Verbruggen, *Appl. Catal. B Environ.*, **2020**, *267*, 118654.

53   L. Gunnarsson, T. Rindzevicius, J. Prikulis, B. Kasemo, M. Käll, S. Zou and G. C. Schatz, *J. Phys. Chem. B*, **2005**, *109*, 1079–1087.

54   Jiang, K. Bosnick, M. Maillard and L. Brus, *J. Phys. Chem. B*, **2003**, *107*, 9964–9972.

55   W. Hou and S. B. Cronin, *Adv. Funct. Mater.*, **2013**, *23*, 1612–1619.

56   A. Bansal, J. S. Sekhon and S. S. Verma, *Plasmonics*, **2014**, *9*, 143–150.

57   S. Linic, U. Aslam, C. Boerigter and M. Morabito, *Nat. Mater.*, **2015**, *14*, 567–576.

58   G. Baffou and R. Quidant, *Chem. Soc. Rev.*, **2014**, *43*, 3898–3907.

59   G. Baffou and R. Quidant, *Laser Photon. Rev.*, **2013**, *7*, 171–187.

60   R. H. M. Groeneveld, R. Sprik and A. Lagendijk, *Phys. Rev. B*, **1992**, *45*, 5079–5082.

61   R. H. M. Groeneveld, R. Sprik and A. Lagendijk, *Phys. Rev. B*, **1995**, *51*, 11433–11445.

62   N. Del Fatti, C. Voisin, M. Achermann, S. Tzortzakis, D. Christofilos and F. Vallée, *Phys. Rev. B*, **2000**, *61*, 16956–16966.

63   C.-K. Sun, F. Vallée, L. H. Acioli, E. P. Ippen and J. G. Fujimoto, *Phys. Rev. B*, **1994**, *50*, 15337–15348.

64   W. S. Fann, R. Storz, H. W. K. Tom and J. Bokor, *Phys. Rev. B*, **1992**, *46*, 13592–13595.

65   G. Tas and H. J. Maris, *Phys. Rev. B*, **1994**, *49*, 15046–15054.

66   T. Shao, X. Wang, H. Dong, S. Liu, D. Duan, Y. Li, P. Song, H. Jiang, Z. Hou, C. Gao and Y. Xiong, *Adv. Mater.*, **2022**, 2202367.

67   C. Wang, O. Ranasingha, S. Natesakhawat, P. R. Ohodnicki, M. Andio, J. P. Lewis and C. Matranga, *Nanoscale*, **2013**, *5*, 6968–6974.

68   T. Hirakawa and P. V Kamat, *Langmuir*, **2004**, *20*, 5645–5647.

69   T. Hirakawa and P. V Kamat, *J. Am. Chem. Soc.*, **2005**, *127*, 3928–3934.

70   K. Awazu, M. Fujimaki, C. Rockstuhl, J. Tominaga, H. Murakami, Y. Ohki, N. Yoshida and T. Watanabe, *J. Am. Chem. Soc.*, **2008**, *130*, 1676–1680.

71   S. W. Verbruggen, *J. Photochem. Photobiol. C Photochem. Rev.*, **2015**, *24*, 64–82.

72   S. W. Verbruggen, M. Keulemans, B. Goris, N. Blommaerts, S. Bals, J. A. Martens and S. Lenaerts, *Appl. Catal. B Environ.*, **2016**, *188*, 147–153.

73   S. W. Verbruggen, M. Keulemans, J. A. Martens and S. Lenaerts, *J. Phys. Chem. C*, **2013**, *117*, 19142–19145.

74   R. Asapu, R.-G. Ciocarlan, N. Claes, N. Blommaerts, M. Minjauw, T. Ahmad, J. Dendooven, P. Cool, S. Bals, S. Denys, C. Detavernier, S. Lenaerts and S. W. Verbruggen, *ACS Appl. Mater. Interfaces*, **2017**, *9*, 41577–41585.

75   R. Asapu, N. Claes, R.-G. Ciocarlan, M. Minjauw, C. Detavernier, P. Cool, S. Bals and S. W. Verbruggen, *ACS Appl. Nano Mater.*, **2019**, *2*, 7, 4067-4074.

76   I. Caretti, M. Keulemans, S. W. Verbruggen, S. Lenaerts and S. Van Doorslaer, *Top. Catal.*, **2015**, *58*, 776–782.

77   S. Linic, P. Christopher and D. B. Ingram, *Nat. Mater.*, **2011**, *10*, 911–921.

78   S. Link and Z. L. Wang, *J. Phys. Chem. B*, **1999**, *103*, 3529–3533.

79   K. J. P. Schouten, Y. Kwon, C. J. M. van der Ham, Z. Qin and M. T. M. Koper, *Chem. Sci.*, **2011**, *2*, 1902–1909.

80   A. Paul, D. Connolly, M. Schulz, M. T. Pryce and J. G. Vos, *Inorg. Chem.*, **2012**, *51*, 1977–1979.

81   J. Rasko and F. Solymosi, *J. Phys. Chem.*, **1994**, *98*, 7147–7152.

82   C.-C. Yang, Y.-H. Yu, B. van der Linden, J. C. S. Wu and G. Mul, *J. Am. Chem. Soc.*, **2010**, *132*, 8398–8406.

83   I. A. Shkrob, N. M. Dimitrijevic, T. W. Marin, H. He and P. Zapol, *J. Phys. Chem. C*, **2012**, *116*, 9461–9471.

84   Y. Ji and Y. Luo, *ACS Catal.*, **2016**, *6*, 2018–2025.

85   V. P. Indrakanti, J. D. Kubicki and H. H. Schobert, *Energy Environ. Sci.*, **2009**, *2*, 745–758.

86   W. H. Koppenol and J. D. Rush, *J. Phys. Chem.*, **1987**, *91*, 4429–4430.

87   K. Tanaka, K. Miyahara and I. Toyoshima, *J. Phys. Chem.*, **1984**, *88*, 3504–3508.

88   S. Sarina, E. Jaatinen, Q. Xiao, Y. M. Huang, P. Christopher, J. C. Zhao and H. Y. Zhu, *J. Phys. Chem. Lett.*, **2017**, *8*, 2526–2534.

89   P. Han, W. Martens, E. R. Waclawik, S. Sarina and H. Zhu, *Part.*

Part. Syst. Charact., **2018**, *35*, 1–16.

90 E. Peiris, S. Sarina, E. R. Waclawik, G. A. Ayoko, P. Han, J. Jia and H.-Y. Zhu, *Angew. Chemie Int. Ed.*, **2019**, *58*, 12032–12036.

91 U. Ulmer, T. Dingle, P. N. Duchesne, R. H. Morris, A. Tavasoli, T. Wood and G. A. Ozin, *Nat. Commun.*, **2019**, *10*, 1–12.

92 M. Abou Asi, L. Zhu, C. He, V. K. Sharma, D. Shu, S. Li, J. Yang and Y. Xiong, *Catal. Today*, **2013**, *216*, 268–275.

93 S. Rodrigues, S. Uma, I. N. Martyanov and K. J. Klabunde, *J. Catal.*, **2005**, *233*, 405–410.

94 C. Hu, Y. Lan, J. Qu, X. Hu and A. Wang, *J. Phys. Chem. B*, **2006**, *110*, 4066–4072.

95 M. R. Elahifard, S. Rahimnejad, S. Haghighi and M. R. Gholami, *J. Am. Chem. Soc.*, **2007**, *129*, 9552–9553.

96 X. Zhou, C. Hu, X. Hu, T. Peng and J. Qu, *J. Phys. Chem. C*, **2010**, *114*, 2746–2750.

97 T. Hasobe, S. Fukuzumi and P. V Kamat, *Angew. Chemie Int. Ed.*, **2006**, *45*, 755–759.

98 A. Kongkanand and P. V Kamat, *ACS Nano*, **2007**, *1*, 13–21.

99 B. Farrow and P. V Kamat, *J. Am. Chem. Soc.*, **2009**, *131*, 11124–11131.

100 D. Eder, *Chem. Rev.*, **2010**, *110*, 1348–1385.

101 Y. K. Kim and H. Park, *Energy Environ. Sci.*, **2011**, *4*, 685–694.

102 W.-J. Ong, L. K. Putri, L.-L. Tan, S.-P. Chai and S.-T. Yong, *Appl. Catal. B Environ.*, **2016**, *180*, 530–543.

103 P. Murugesan, S. Narayanan, M. Manickam, P. K. Murugesan and R. Subbiah, *Appl. Surf. Sci.*, **2018**, *450*, 516–526.

104 P. Zhou, J. Yu and M. Jaroniec, *Adv. Mater.*, 2014.

105 Z. Haijin, Li; Wenguang, Tu; Yong, Zhou; and Zhigang, .

106 M. Humayun, Q. Fu, Z. Zheng, H. Li and W. Luo, *Appl. Catal. A Gen.*, **2018**, *568*, 139–147.

107 Z. Q. He, D. Wang, H. Y. Fang, J. M. Chen and S. Song, *Nanoscale*, **2014**, *6*, 10540–10544.

108 D. Wang, Y. Yu, Z. Zhang, H. Fang, J. Chen, Z. He and S. Song, *Environ. Sci. Pollut. Res.*, **2016**, *23*, 18369–18378.

109 J. Mao, K. Li and T. Peng, *Catal. Sci. Technol.*, **2013**, *3*, 2481–2498.

110 J. Zhao, B. Liu, L. Meng, S. He, R. Yuan, Y. Hou, Z. Ding, H. Lin, Z. Zhang, X. Wang and J. Long, *Appl. Catal. B Environ.*, **2019**, *256*, 117823.

111 N. Blommaerts, N. Hoeven, D. Arenas Esteban, R. Campos, M. Mertens, R. Borah, A. Glisenti, K. De Wael, S. Bals, S. Lenaerts, S. W. Verbruggen and P. Cool, *Chem. Eng. J.*, **2021**, *410*, 128234.

112 S. Feng, M. Wang, Y. Zhou, P. Li, W. Tu and Z. Zou, *APL Mater.*, **2015**, *3*, 104416.

113 B. Yu, Y. Zhou, P. Li, W. Tu, P. Li, L. Tang, J. Ye and Z. Zou, *Nanoscale*, **2016**, *8*, 11870–11874.

114 M. Dilla, A. Pougin and J. Strunk, *J. Energy Chem.*, **2017**, *26*, 277–283.

115 J. Low, S. Qiu, D. Xu, C. Jiang and B. Cheng, *Appl. Surf. Sci.*, **2018**, *434*, 423–432.

116 L. Collado, A. Reynal, F. Fresno, M. Barawi, C. Escudero, V. Perez-Dieste, J. M. Coronado, D. P. Serrano, J. R. Durrant and V. A. de la Peña O'Shea, *Nat. Commun.*, **2018**, *9*, 4986.

117 K. Mudiyanselage, S. D. Senanayake, L. Feria, S. Kundu, A. E. Baber, J. Graciani, A. B. Vidal, S. Agnoli, J. Evans, R. Chang, S. Axnanda, Z. Liu, J. F. Sanz, P. Liu, J. A. Rodriguez and D. J. Stacchiola, *Angew. Chemie Int. Ed.*, **2013**, *52*, 5101–5105.

118 H. Bluhm, M. Hävecker, A. Knop-Gericke, E. Kleimenov, R. Schlögl, D. Teschner, V. I. Bukhtiyarov, D. F. Ogletree and M. Salmeron, *J. Phys. Chem. B*, **2004**, *108*, 14340–14347.

119 S. Zafeiratos, F. Paloukis, G. Papakonstantinou, D. Teschner, M. Hävecker, E. Vass, P. Schnörch, A. Knop-Gericke, R. Schlögl, B. Moreno, E. Chinarro, J. R. Jurado and S. G. Neophytides, *Catal. Today*, **2010**, *157*, 250–256.

120 G. Ketteler, S. Yamamoto, H. Bluhm, K. Andersson, D. E. Starr, D. F. Ogletree, H. Ogasawara, A. Nilsson and M. Salmeron, *J. Phys. Chem. C*, **2007**, *111*, 8278–8282.

121 B. Xin, L. Jing, Z. Ren, B. Wang and H. Fu, *J. Phys. Chem. B*, **2005**, *109*, 2805–2809.

122 N. Ohtsu, N. Masahashi, Y. Mizukoshi and K. Wagatsuma, *Langmuir*, **2009**, *25*, 11586–11591.

123 Q. Liu, Y. Han, J. Cai, E. J. Crumlin, Y. Li and Z. Liu, *Catal. Letters*, **2018**, *148*, 1686–1691.

124 Y. Toda, H. Hirayama, N. Kuganathan, A. Torrisi, P. V Sushko and H. Hosono, *Nat. Commun.*, **2013**, *4*, 2378.

125 N. M. Dimitrijevic, B. K. Vijayan, O. G. Poluektov, T. Rajh, K. A. Gray, H. He and P. Zapol, *J. Am. Chem. Soc.*, **2011**, *133*, 3964–3971.

126 D. E. Starr, E. K. Wong, D. R. Worsnop, K. R. Wilson and H. Bluhm, *Phys. Chem. Chem. Phys.*, **2008**, *10*, 3093–3098.

127 D. Hong, L.-M. Lyu, K. Koga, Y. Shimoyama and Y. Kon, *ACS Sustain. Chem. Eng.*, **2019**, *7*, 18955–18964.

128 W. Hou, W. H. Hung, P. Pavaskar, A. Goeppert, M. Aykol and S. B. Cronin, *ACS Catal.*, **2011**, *1*, 929–936.

129 R. Wang, J. Shen, K. Sun, H. Tang and Q. Liu, *Appl. Surf. Sci.*, **2019**, *493*, 1142–1149.

130 F. Khatun, A. Abd Aziz, L. C. Sim and M. U. Monir, *J. Environ. Chem. Eng.*, **2019**, *7*, 103233.

131 S. Zeng, E. Vahidzadeh, C. G. VanEssen, P. Kar, R. Kisslinger, A. Goswami, Y. Zhang, N. Mahdi, S. Riddell, A. E. Kobryn, S. Gusarov, P. Kumar and K. Shankar, *Appl. Catal. B Environ.*, **2020**, *267*, 118644.

132 A. Ziarati, A. Badiei, R. Luque, M. Dadras and T. Burgi, *ACS Sustain. Chem. Eng.*, **2020**, *8*, 3689–3696.

133 Y. Ma, X. Yi, S. Wang, T. Li, B. Tan, C. Chen, T. Majima, E. R. Waclawik, H. Zhu and J. Wang, *Nat. Commun.*, **2022**, *13*, 1400.

134 Z. Zhang, Y. Huang, K. Liu, L. Guo, Q. Yuan and B. Dong, *Adv. Mater.*, **2015**, *27*, 5906–5914.

135 X. Jiang, J. Huang, Z. Bi, W. Ni, G. Gurzadyan, Y. Zhu and Z. Zhang, *Adv. Mater.*, **2022**, *34*, 14, 2109330.

136 J. Bian, Y. Qu, X. Zhang, N. Sun, D. Tang and L. Jing, *J. Mater. Chem. A*, **2018**, *6*, 11838–11845.

137 S. Bera, J. E. Lee, S. B. Rawal and W. I. Lee, *Appl. Catal. B Environ.*, **2016**, *199*, 55–63.

138 B. D. Mankidy, B. Joseph and V. K. Gupta, *Nanotechnology*, **2013**, *24*, 405402.

139 J. Z. Y. Tan, Y. Fernández, D. Liu, M. Maroto-Valer, J. Bian and X. Zhang, *Chem. Phys. Lett.*, **2012**, *531*, 149–154.

140 H. Lee, S. In and M. W. Horn, *Thin Solid Films*, **2014**, *565*, 105–110.

141 T. Kulandaivalu, A. R. Mohamed, K. A. Ali and M. Mohammadi, *Renew. Sustain. Energy Rev.*, **2020**, *134*, 110363.

142 H. Li, Y. Gao, Z. Xiong, C. Liao and K. Shih, *Appl. Surf. Sci.*, **2018**, *439*, 552–559.

143 X. Li, C. Liu, D. Wu, J. Li, P. Huo and H. Wang, *Chinese J. Catal.*, **2019**, *40*, 928–939.

144 F. Li, H. Zhou, J. Fan and Q. Xiang, *J. Colloid Interface Sci.*, **2020**, *570*, 11–19.

145 S. Wan, M. Chen, M. Ou and Q. Zhong, *J. CO2 Util.*, **2019**, *33*, 357–364.

146 M. Gu, D. Liu, T. Ding, X. Liu, T. Chen, X. Shen and T. Yao, *Dalt. Trans.*, **2021**, *50*, 6076–6082.

147 J. F. Liao, Y. T. Cai, J. Y. Li, Y. Jiang, X. D. Wang, H. Y. Chen and D. Bin Kuang, *J. Energy Chem.*, **2020**, *53*, 309–315.

148 H. Robatjazi, H. Zhao, D. F. Swearer, N. J. Hogan, L. Zhou, A. Alabastri, M. J. McClain, P. Nordlander and N. J. Halas, *Nat. Commun.*, **2017**, *8*, 27.

149 S. Kawamura, M. C. Puscasu, Y. Yoshida, Y. Izumi and G. Carja, *Appl. Catal. A Gen.*, **2015**, *504*, 238–247.

150 T. Butburee, Z. Sun, A. Centeno, F. Xie, Z. Zhao, D. Wu, P. Peerakiatkhajohn, S. Thaweesak, H. Wang and L. Wang, *Nano Energy*, **2019**, *62*, 426–433.

151 X. Cheng, P. Dong, Z. Huang, Y. Zhang, Y. Chen, X. Nie and X. Zhang, *J. CO2 Util.*, **2017**, *20*, 200–207.

152 H. Zhao, X. Zheng, X. Feng and Y. Li, *J. Phys. Chem. C*, **2018**, *122*, 18949–18956.

153 D. M. Wood, *Phys. Rev. Lett.*, **1981**, *46*, 749.

154 W. Kim, T. Tachikawa, T. Majima and W. Choi, *J. Phys. Chem. C*, **2009**, *113*, 10603–10609.

155 C. Prasittichai and J. T. Hupp, *J. Phys. Chem. Lett.*, **2010**, *1*, 1611–1615.

156 H. Zhao, J. Chen, G. Rao, W. Deng and Y. Li, *Appl. Surf. Sci.*, **2017**, *404*, 49–56.

157 K. Yee, *IEEE Trans. Antennas Propag.*, **1966**, *14*, 302–307.

158 K. Wang, J. Lu, Y. Lu, C. H. Lau, Y. Zheng and X. Fan, *Appl. Catal. B Environ.*, **2021**, *292*, 120147.

159 A. Wang, S. Wu, J. Dong, R. Wang, J. Wang, J. Zhang, S. Zhong and S. Bai, *Chem. Eng. J.*, **2021**, *404*, 127145.

160 R. Li, W. H. Cheng, M. H. Richter, J. S. Duchene, W. Tian, C. Li and H. A. Atwater, *ACS Energy Lett.*, **2021**, *6*, 1849–1856.

161 Q. Shi, Z. Li, L. Chen, X. Zhang, W. Han, M. Xie, J. Yang and L. Jing, *Appl. Catal. B Environ.*, **2019**, *244*, 641–649.

162 M. Xie, X. Fu, L. Jing, P. Luan, Y. Feng and H. Fu, *Adv. Energy Mater.*, **2014**, *4*, 1300995.

163 J. Wu, Y. Huang, W. Ye and Y. Li, *Adv. Sci.*, **2017**, *4*, 1700194.

164 M. Xie, Y. Feng, X. Fu, P. Luan and L. Jing, *J. Alloys Compd.*, **2015**, *631*, 120–124.

165 S. A. Mahyoub, A. Hezam, F. A. Qaraah, K. Namratha, M. B. Nayan, Q. A. Drmosh, D. Ponnamma and K. Byrappa, *ACS Appl. Energy Mater.*, **2021**, *4*, 3544–3554.

166 Y. Zhou, L. Zhang and W. Wang, *Nat. Commun.*, **2019**, *10*, 506.

167 H. Li, S. Gan, H. Wang, D. Han and L. Niu, *Adv. Mater.*, **2015**, *27*, 6906–6913.

168 P. Wang, B. Huang, X. Qin, X. Zhang, Y. Dai and M.-H. Whangbo, *Inorg. Chem.*, **2009**, *48*, 10697–10702.

169 S. Yang, Y. Gong, J. Zhang, L. Zhan, L. Ma, Z. Fang, R. Vajtai, X. Wang and P. M. Ajayan, *Adv. Mater.*, **2013**, *25*, 2452–2456.

170 J. Zhang, M. Zhang, C. Yang and X. Wang, *Adv. Mater.*, **2014**, *26*, 4121–4126.

171 M. S. A. Sher Shah, W.-J. Kim, J. Park, D. K. Rhee, I.-H. Jang, N.-G. Park, J. Y. Lee and P. J. Yoo, *ACS Appl. Mater. Interfaces*, **2014**, *6*, 20819–20827.

172 M. Zhu, P. Chen and M. Liu, *ACS Nano*, **2011**, *5*, 4529–4536.

173 W. Tu, Y. Zhou and Z. Zou, *Adv. Mater.*, **2014**, *26*, 4607–4626.

174 C. An, J. Wang, W. Jiang, M. Zhang, X. Ming, S. Wang and Q. Zhang, *Nanoscale*, **2012**, *4*, 5646–5650.

175 B. Cai, J. Wang, S. Gan, D. Han, Z. Wu and L. Niu, *J. Mater. Chem. A*, **2014**, *2*, 5280–5286.

176 E. Liu, Y. Hu, H. Li, C. Tang, X. Hu, J. Fan, Y. Chen and J. Bian, *Ceram. Int.*, **2015**, *41*, 1049–1057.

177 J. C. S. Wu, *Catal. Surv. from Asia*, **2009**, *13*, 30–40.

178 E. Liu, L. Qi, J. Bian, Y. Chen, X. Hu, J. Fan, H. Liu, C. Zhu and Q. Wang, *Mater. Res. Bull.*, **2015**, *68*, 203–209.

179 Z. Wang, H. Song, H. Pang, Y. Ning, T. D. Dao, Z. Wang, H. Chen, Y. Weng, Q. Fu, T. Nagao, Y. Fang and J. Ye, *Appl. Catal. B Environ.*, **2019**, *250*, 10–16.

180 K. Larmier, W.-C. Liao, S. Tada, E. Lam, R. Verel, A. Bansode, A. Urakawa, A. Comas-Vives and C. Copéret, *Angew. Chemie Int. Ed.*, **2017**, *56*, 2318–2323.

181 S. Kattel, P. Liu and J. G. Chen, *J. Am. Chem. Soc.*, **2017**, *139*, 9739–9754.

182 R. Yadav, V. Amoli, J. Singh, M. K. Tripathi, P. Bhanja, A. Bhaumik and A. K. Sinha, *J. CO2 Util.*, **2018**, *27*, 11–21.

183 M. Kosmulski, *J. Colloid Interface Sci.*, **2009**, *337*, 439–448.

184 I. Arnaud, J.-P. Abid, C. Roussel and H. H. Girault, *Chem. Commun.*, **2005**, 787–788.

185 J. Becerra, D. T. Nguyen, V. N. Gopalakrishnan and T. O. Do, *ACS Appl. Energy Mater.*, **2020**, *3*, 7659–7665.

186 H. Yu, C. Sun, Y. Xuan, K. Zhang and K. Chang, *Chem. Eng. J.*, **2022**, *430*, 132940.

Entry for the Table of Contents
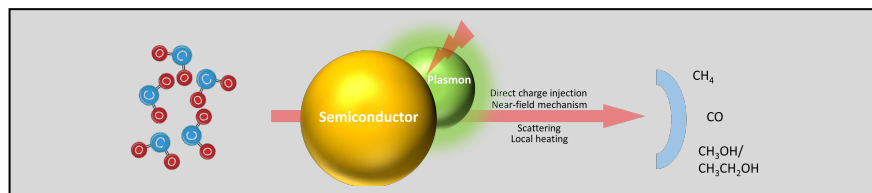
This review provides a case-based overview of recent developments in the field of plasmon-enhanced semiconductor photocatalytic CO_2 conversion, potentially a highly sustainable CO_2 reduction technology since it can operate entirely under solar light. The highly focused manuscript on plasmonic nanoparticle-semiconductor systems, is classified based on product selectivity, thus elucidating common trends and future research opportunities.